High Precision Spacecraft Formation Control (HORES)

DLR contract No. 50 JR 0648

Part I:

Analysis of fringe sensor principles and algorithms

Signature Field		
Prepared by:	Hartmut Jörck, Klaus Ergenzinger, Michael Kersten	
Verified by:	Klaus Ergenzinger, Michael Kersten, Hartmut Jörck	
Approved by:	Michael Kersten, Hartmut Jörck, Klaus Ergenzinger	

Astrium GmbH
88039 Friedrichshafen
Telephone: (07545) 800
Telefax: (07545) 84411

CHANGE RECORD

ISSUE	DATE	SECTION	DESCRIPTION OF CHANGE
1	29.11.06	all	First formal issue

Astrium GmbH
88039 Friedrichshafen
Telephone: (07545) 800
Telefax: (07545) 84411

TABLE OF CONTENTS

Astrium GmbH
88039 Friedrichshafen
Telephone: (07545) 800
Telefax: (07545) 84411

Astrium GmbH
88039 Friedrichshafen
Telephone: (07545) 800
Telefax: (07545) 84411

1 Scope and Introduction

1.1 Scope

This document deals with the analysis of existing fringe sensor principles suitable for measuring the optical path differences between the arms of spaceborne interferometers distributed over several spacecraft flying in formation to sub-nanometer accuracy. In addition, it also addresses the requirements for such sensors which originate from scientific applications.

This work was funded by the German Aerospace Institute (Deutsches Zentrum für Luft- und Raumfahrt) under contract No. 50 JR 0648.

1.2 Introduction

DARWIN

The DARWIN mission was proposed to ESA in 1993 and is now a promising candidate mission for the "Cosmic Vision 2015-2025" program. The mission's main objective is the search for signs of life as we know it on extrasolar planets orbiting suns in distant solar systems.

DARWIN is a space-based free-flying infrared interferometer with four telescope carrying collector spacecraft and one central beam combiner spacraft, positioned in an L2 orbit 1.5 million kilometres away from the earth with baselines, i.e., distances between the telescope spacecraft, ranging from 15 m to 250 m. DARWIN features two distinctive observing modes:

- a nulling mode dedicated to the detection and spectroscopy of extrasolar planets around nearby main sequence stars (located at distances within ≅ 5-25 pc),
- an imaging mode to be used for general astrophysics with angular resolution in the milli-arcsecond scale.

More precisely, the ultimate goal of the nulling mode is to carry out remote spectroscopy of extrasolar planets' atmospheres in the 6.5-20 microns region, looking for absorption lines of H_2O, CH_4, O_3, and CO_2. The simultaneous detection of water and ozone is considered as a strong evidence for the presence of life based on photochemistry.

The difficulty to achieve this observation goal lies in the brightness and proximity of the central star that is orbited by an exoplanet. It is therefore necessary to suppress this star light that is by six orders of magnitude brighter than the exo-planet. The way chosen for DARWIN to suppress the star light in favour of the light from the exoplanet is to use a nulling interferometer in which ideally the light from the on-axis star is subject to destructive interference so that only the planet signal remains.

The obvious advantages of space-based free-flying interferometer configurations are the long and variable baselines yielding excellent spatial resolution, and absence of thermal background radiation. In particular the latter topic is the main reason why ground based instruments are severely limited in the mid infrared wavelength range as the telescope facilities and the surrounding air are "glowing" at

Astrium GmbH
88039 Friedrichshafen
Telephone: (07545) 800
Telefax: (07545) 84411

room temperature. Candidate earth-like planets are characterized by temperatures around 300 K and show a transmission peak at 10 µm, the main observing wavelength of DARWIN.

The high level objectives of the DARWIN mission are to perform a survey of nearby stars for terrestrial planets within the habitable zone, to study in detail any planets found, and to analyse any planetary atmosphere for signs of biological activity. The mission duration is at least 5 years, with a goal of 10 years including sufficient propellant mass margin.

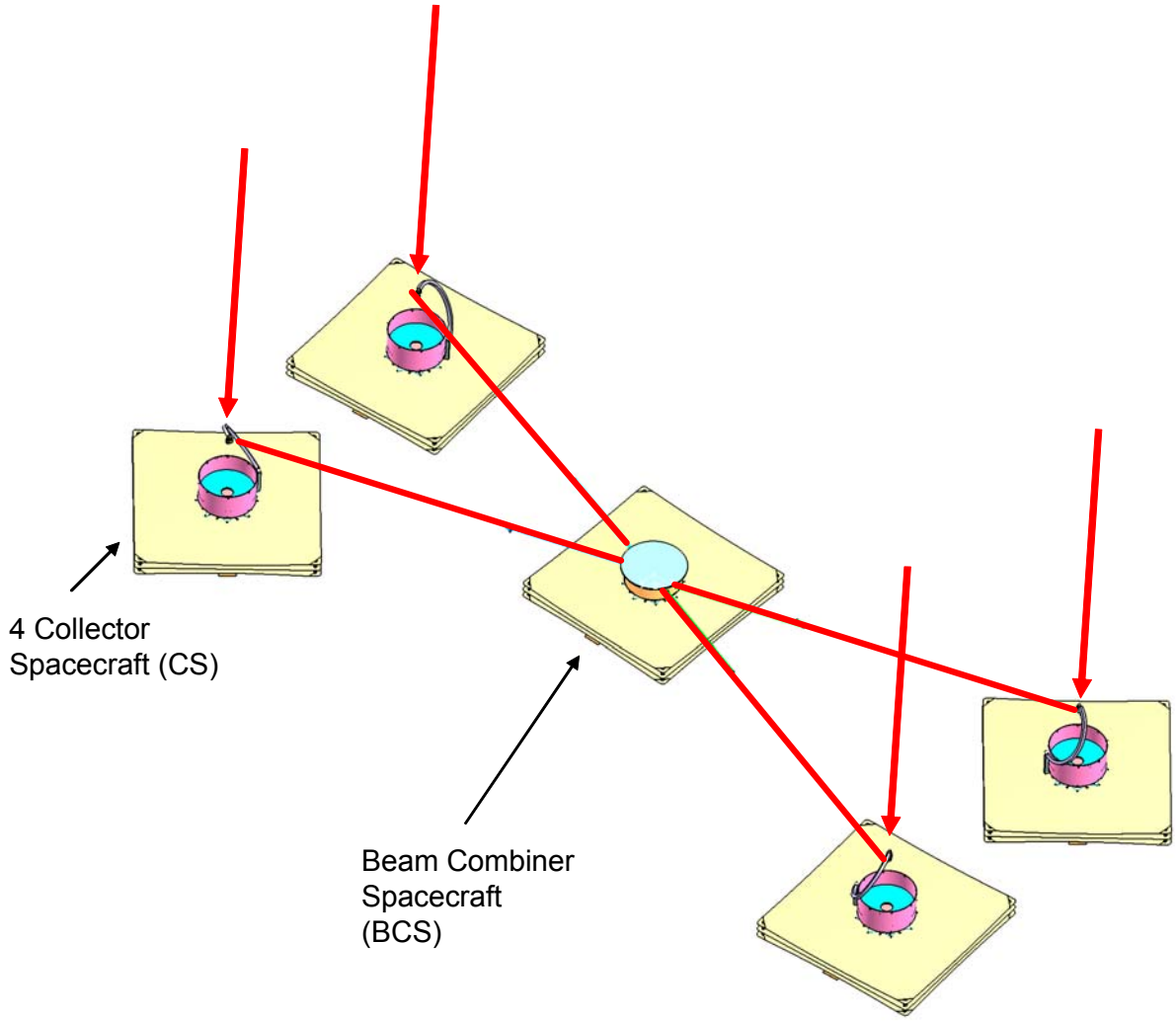

Figure 1.2-1 Layout for DARWIN free-flying formation consisting of four telescope carrying collector spacecraft (CS) and one central beam combiner spacecraft (BCS). Because of its shape this configuration is called "X-Array". The red arrows indicate the four light paths of star light to the beam combiner spacecraft.

Astrium GmbH
88039 Friedrichshafen
Telephone: (07545) 800
Telefax: (07545) 84411

Fringe Sensors

Four beams from four free-flying telescopes must be brought to perfect (destructive) interference in the central beam combiner spacecraft. Therefore all four beams must match ideally to very stringent requirements on beam optical path lengths (nanometer) and beam tip/tilt (tens of milliarcseconds on sky). Such a performance cannot be achieved by pure formation flying of the individual spacecraft, but dedicated actuators and sensors are required.

The actuators used for optical pathlength adjustment of the four beams are optical delay lines (ODLs) and the actuators for tip/tilt adjustment are fine steering mirrors. The sensors for measuring optical path length differences (OPDs) between beams are called fringe sensors. The readings of fine pointing sensors are used for control of the fine steering mirrors.

The term "fringe sensor" (Interferenzstreifensensor) comes from the measurement principle of those sensors that is based on the analysis of the interference pattern resulting from the (partially) coherent superposition of several beams. These interference patterns are commonly called “fringes" (Interferenzstreifen).

For DARWIN the fringe sensor unit(s) must provide sensor signals with outstanding accuracy in order to allow the co-phasing in terms of optical path length differences (OPDs) of all four beams to nanometer level.

Objective

Objective of this study activity shall be to implement a detailed model for candidate fringe sensor concepts, analyzing:

- Four (4) input beams perturbed in beam lateral displacement, beam tip/tilt, OPD, and higher order wavefront errors
- Sensor signal reconstruction quality for (at least) OPD and possibly tip/tilt in terms of bias, accuracy, and noise
- As function of photon noise for DARWIN target stars typical and worst cases

All parameters used in this report are outcome of the recently completed Astrium GmbH "DARWIN System Assessment Study" for ESA. In the frame work of this study the DARWIN baseline configuration was decided in April 2006 to be the planar so-called X-Array with four collector spacecraft (CS), with an array aspect ratio of 3:1 and with nulling baselines ranging from 15 m up to 250 m. The nulling baseline is understood to be the distance between a CS and its nearest neighbour CS.

To define and validate a proper fringe sensor unit (FSU) design and corresponding reconstruction algorithms is the main goal of this study phase.

Crosstalk

A critical criterion for fringe sensor concepts is their susceptibility to crosstalk between different beam perturbations. Crosstalk is contributing to a higher or lesser degree to the measurement error. Most

Astrium GmbH
88039 Friedrichshafen
Telephone: (07545) 800
Telefax: (07545) 84411

fringe sensor algorithms assume implicitly but incorrectly that the only beam perturbation present is OPD that is to be sensed by the FSU. The other beam "rigid body" degrees of freedom like tip/tilt, lateral beam displacement, beam rotation, and higher order Zernikes are often *not* taken into account, but considered to be perfectly eliminated by, e.g. tip/tilt control.

Accuracy

But this correction is never perfect of course, and in the accuracy range of below 1 nm for DARWIN, there are non-negligible residual OPD errors through some kind of crosstalk between these errors. Currently the major unknown of state-of-the-art fringe sensor units is the tolerance to lateral beam displacement.

1.3 Document Structure

The document structure is as follows:

Section 2 states all references which are used to perform the study.

Section 3 deals with the boundary conditions and requirements for the DARWIN fringe sensor unit as driven by DARWIN system aspects.

Section 4 analyzes principal fringe sensor working principles and discusses two candidate approaches in further detail.

Section 5 presents the results of a dedicated simulation test campaign with these candidate approaches.

Section 6 summarizes the results achieved and provides recommendations for future work.

Astrium GmbH
88039 Friedrichshafen
Telephone: (07545) 800
Telefax: (07545) 84411

1.4 Abbreviations

The following abbreviations are used within this document.

Abbreviation	Description
BCS	Beam combiner spacecraft
CCD	Charge-coupled device
CS	Collector spacecraft carrying a telescope
ESA	European Space Agency
FDIR	Fault detection, isolation, and recovery
FFT	Fast Fourier transform
FSU	Fringe sensor unit
HORES	Hochpräzise Regelung für Satellitenformationen (high precision spacecraft formation control)
IR	Infrared
ISD	Inter-spacecraft distance
LISA	Laser Interferometer Space Antenna
LBTI	Large binocular telescope interferometer
MIDI	Mid infrared interferometer
MPIA	Max-Planck institute for astronomy, Heidelberg Germany
MPIfR	Max-Planck institute for radioastronomy, Bonn Germany
MRD	DARWIN mission requirements document [MRD]
OPD	Optical path difference
ODL	Optical delay line
OTF	Optical transfer function
PRIMA	Phase reference imaging and astrometry
RF	Radio-frequency
RMS	Root mean squares
SC	Spacecraft
SNR	Signal to noise ratio
TRP	Technology research program of ESA
TTN	Three telescope nuller
VLTI	Very Large Telescope interferometer
ZPD	Zero path difference

Astrium GmbH
88039 Friedrichshafen
Telephone: (07545) 800
Telefax: (07545) 84411

2 Documents

The documents applicable or related to this study are listed hereafter.

2.1 Applicable Documents

ID	TITLE
[AD-01]	Astrium GmbH Zuwendungsantrag Nr. A.2006-4288-0-1, Hochpräzise Regelung für Satelliten-Formationen

2.2 Reference Documents

ID	TITLE
[TN4]	Technical note 4, “DARWIN Payload Design”, V1.1, Astrium, November 2006
[MRD]	DARWIN Mission requirements document V1.1, ESA, Sci-A/2005/287/Darwin/DMS, September 2005
[Baron]	F. Baron, F. Cassaing, L. Mugnier : "Cophasage des pupilles d'un télescope multi-pupilles", 19th GRETSI Symposium on Signal and Image Processing, Paris, September 8 -11, 2003
[Goodman]	Joseph W. Goodman: "Introduction to Fourier Optics", 2nd edition, McGraw-Hill 1996
[Fienup1982]	J.R. Fienup: "Phase retrieval algorithms: a comparison", Appl.Opt., Vol.21, No.15, pp. 2758, 1982
[Bely2003]	P. Bely: “The design and construction of large optical telescopes”, Springer 2003
[AMBER99]	ESO AMBER Conceptual Design Review, AMB-REP-004, 1999
[PDD2005]	“Payload Definition Document for DARWIN” ESA 2005
[Paxman]	R. Paxman et al.: “Joint estimation of object and aberrations by using phase diversity”, J.Opt.Soc.Am. A Vol.9, No.7, July 1992

Astrium GmbH
88039 Friedrichshafen
Telephone: (07545) 800
Telefax: (07545) 84411

3 System Requirements

3.1 Introduction

Within the beam combiner spacecraft, the four beams from the four collector spacecraft are spectrally divided. The visible spectrum is sent to the DARWIN science beam metrology, i.e. fringe sensor and pointing sensor. The mid-IR spectrum from 6.5 to 20 µm carries the scientific signal, i.e. the photons from the potential exoplanet, and is sent to the destructive nulling core. These mid-IR beams are to be destructively superimposed in the mid-IR nulling optical assembly, and this perfectly destructive interference constitutes the actual performance drivers for DARWIN.

3.1.1 Overall DARWIN metrology approach and beam combiner design

Beyond this science beam metrology, three further metrology functional chains are required for DARWIN, as summarized below.

RF metrology and star tracker	Coarse inter-SC metrology for autonomous formation control in deployment normal mode
Science beam metrology in visible	Ultimate metrology performance within DARWIN Nulling science mode, for all relevant 5 DoF per beam
Optical/Laser metrology	To bridge the performance gap from coarse inter-SC metrology performance to within the capture range of science beam visible metrology
Science beam Mid-IR Nulling calibration and stabilization	Calibration and Control of the Mid-IR Nulling optical assembly

Tab. 3-1 All four DARWIN metrology functional chains

Radio-frequency (RF) metrology constitutes a coarse formation control only, in the mm and arcsecond accuracy regime.

Optical/Laser metrology is subsequently used for acquisition of the actual DARWIN science modes in the nanometer/milliarcsec regime, which are subsequently stabilized by the DARWIN science beam metrology in the visible.

Finally a vey precise calibration and adjustment of the Mid-IR science channel to the visible science beam metrology is further required.

The central and most demanding unit of the DARWIN science beam metrology consists of the DARWIN FSU, which is the focus of this study activity.

Astrium GmbH
88039 Friedrichshafen
Telephone: (07545) 800
Telefax: (07545) 84411

The actual arrangement of the DARWIN beam combiner spacecraft payload is shown below.

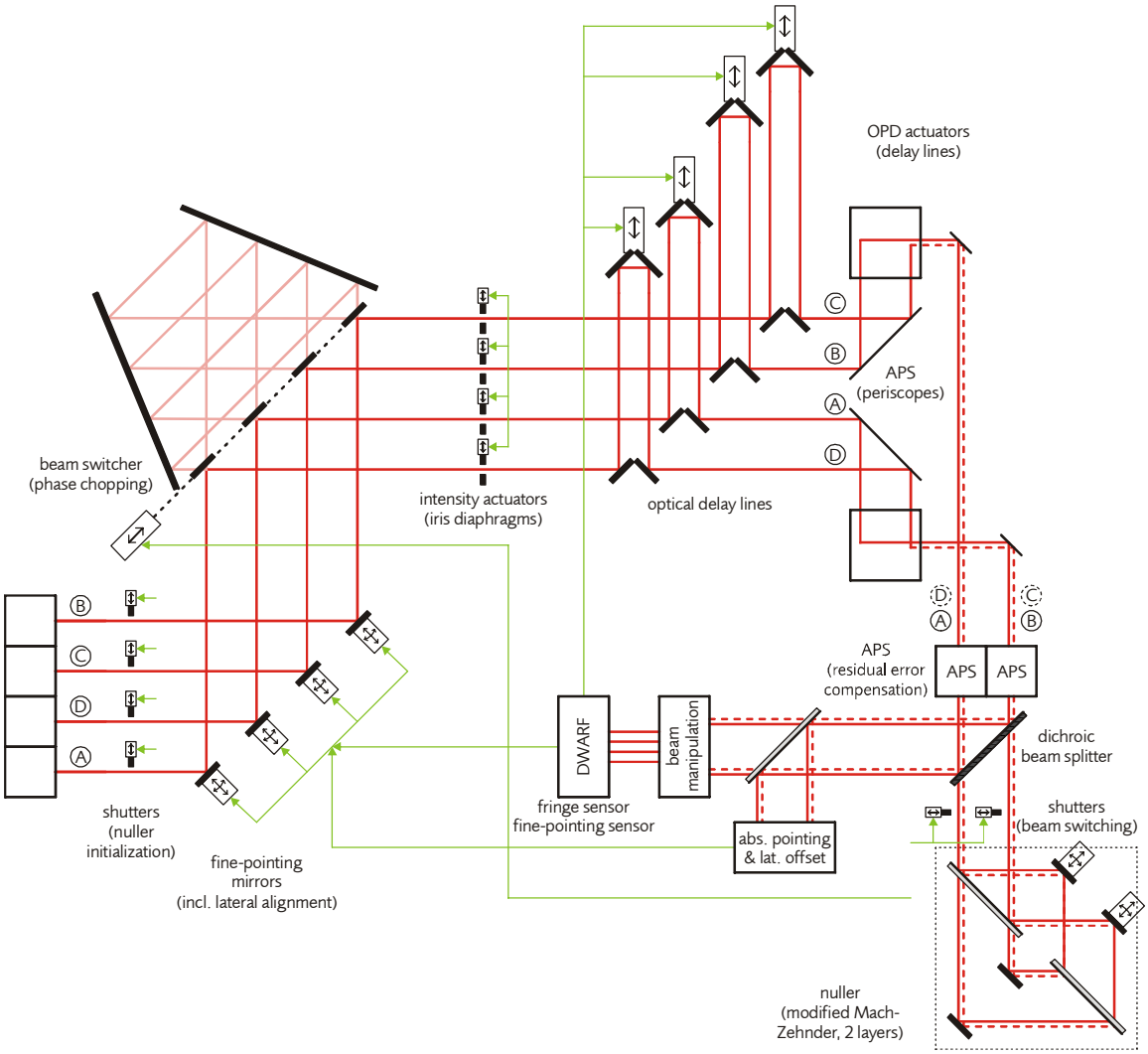

Figure 3.1-1 Concept optical layout of DARWIN science beam metrology and control, with Mid-IR Nulling section only sketched through initial Mach-Zehnder core

3.1.2 DARWIN OPD and fine pointing metrology

This section discusses DARWIN science beam metrology and control on the visible spectrum of the DARWIN science beams. In order to achieve utmost control of the DARWIN Mid-IR science beams, DARWIN science beam metrology controls all five relevant degrees of freedom of each of the individual beams (namely optical path length, tip/tilt, and lateral displacements) in the most demanding Nulling science mode.

Astrium GmbH
88039 Friedrichshafen
Telephone: (07545) 800
Telefax: (07545) 84411

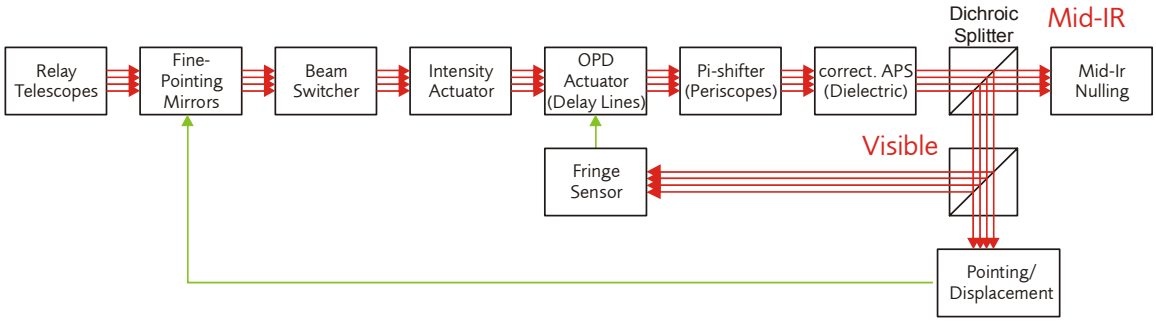

Figure 3.1-2 Functional chain of DARWIN science beam metrology and control. Visible spectrum is separated at a dichroic mirror towards fringe sensor and pointing sensor. The use of a dedicated displacement sensor is optional and depends on actual overall system approach.

3.1.3 DARWIN key parameters for science beam metrology

The following table presents the control requirement that have been derived form the top level nulling performance requirements of stellar light suppression of 1.5×10^{-5} as of the DARWIN Mission Requirements Document [MRD]. Explicitly the properties of a 2x2 beam nulling scheme (the X-Array) and coaxial beam combination are taken into account. Consequently the below numbers are implementation dependent with respect to

- 2x2 beam nulling versus three-beam nulling (TTN)
- Coaxial beam combination versus multiaxial beam combination

Whereas the DARWIN [MRD] talks in terms of nulldepth as well as phase and intensity fluctuations allowed, the breakdown onto all five degrees of freedom per individual beam has been described in detail in [TN4] of the Astrium DARWIN System Assessment Study.

The following performance requirements on OPD, tip/tilt, and lateral beam displacement fulfill the DARWIN MRD requirements.

	Values	**Comment**
OPD	RMS : 1 nm RMS Bias : 2.5 nm	
Tip/tilt (on 200mm beam before beam compressors in central SC)	RMS :70mas Bias : 70mas	Tip/tilt measured corresponds to BCS-CS relative pointing
Lateral beam displacement (on 200mm beam before beam compressors in central SC))	RMS: 3.5 mm Bias: 2.5 mm	0.175 mm on 10 mm beam 0.125 mm on 10 mm beam

Tab. 3-2 Science mode control requirements.

Astrium GmbH
88039 Friedrichshafen
Telephone: (07545) 800
Telefax: (07545) 84411

Absolute requirements on lateral displacements and tilts scale with beam diameter considered. The current Astrium setup as of the DARWIN System Assessment Study foresees 10 mm beam diameter within the DARWIN beam combiner.

To ensure these stringent control performances, a dual stage architecture is proposed for both OPD and tip/tilt control. A coarse control is performed at formation level through spacecraft *attitude* and *position*. Fine control stages inside the beam combiner spacecraft using optical delay lines and fine steering mirrors then ensure the final control performance.

From the previous top-level requirements, the below allocations have been derived for the various control loops. The results are presented here below:

	Allocation	**Origin/comment**
Lateral position of SC	0.3 mm RMS	ODL stroke (2mm allocation for dynamic control)
Longitudinal position of SC	0.3 mm RMS	ODL stroke (2mm allocation for dynamic control)
BCS absolute attitude	RMS 1 arcsec	Lateral beam displacement (462 m ISD). Can be relaxed to 2” for a 230m ISD.
BCS-CS beam relative pointing	RMS 1 arcsec	Lateral beam displacement (462m ISD). Can be relaxed to 1.6” for a 230m ISD.(mirror stroke then becomes the driver).
CS absolute attitude pointing (Z axis)	RMS 1 arcsec	Design goal, No strict constraint on that axis, as no optic amplification factor apply.
OPD control	RMS : 1 nm	
Tip/tilt control	RMS : 70 milliarcsec	On 200 mm beam

Tab. 3-3 Coarse and fine control loop performance allocations for the DARWIN science mode

Extensive control loop simulations in the Astrium DARWIN System Assessment Study (by A. Villien) provided below detailed results. Though these are detailed results of a detailed simulation, they are only specific for a given assumption on the environmental noise for DARWIN. The uncertainties therein in the model input certainly dominate the uncertainties of the model itself. Therefore the below numbers are all to be considered as order of magnitude analysis results only.

To achieve the required nested control performance, the following sensor performance requirements must be imposed:

Astrium GmbH
88039 Friedrichshafen
Telephone: (07545) 800
Telefax: (07545) 84411

Sensor	Noise specifications	Comments
Fringe Sensor	0.51 nm RMS @50Hz	Equivalent to 0.23 nm RMS @10 Hz, truly photon-noise limited
Startracker on CS & BCS	1000 mas/√Hz	
Fine pointing sensor	30 mas/√Hz	On the 200 mm ∅ beam
Fine lateral and longitudinal position metrology	1000 µm/√Hz	

Tab. 3-4 Sensor performance requirements for the DARWIN science mode

And the hereafter shown control loop cut-off frequencies turned out to be optimum in minimizing the requirements on thruster noise etc.

Control loop	Cut-off frequency
Relative position	5e-4 Hz
BCS and CS attitude	5e-3 Hz
Fine pointing	1e-1Hz
OPD control	5 Hz

Tab. 3-5 Control loop cut-off frequencies

As one conclusion, if all these performance numbers can be met, no dedicated second stage control loop is required for beam lateral displacement, but instead individual spacecraft attitude and position control is sufficient. This special realization will be used as baseline throughout the following.

To conclude, four types of interleaved control loops are required for DARWIN:

- Individual spacecraft attitude control loops for each CS and BCS individually
- CS position control loops (longitudinal and lateral) relative to BCS
- Control loops for fine-steering mirrors within BCS
- OPD control loops within BCS

The two latter ones are done on the DARWIN science beams themselves.

Internal microvibration allowances on board assuming a 1000kg spacecraft

The above control loop sizing is based on the following internal microvibration allowances per spacecraft in the DARWIN science mode:

Astrium GmbH
88039 Friedrichshafen
Telephone: (07545) 800
Telefax: (07545) 84411

FEEPs/micropropulsion	3 µN/√Hz per axis
ODL (command)	1 nm/s/√Hz
Further microvibrations, e.g. from cooler	4 µN/√Hz

Tab. 3-6 Microvibration allocations per spacecraft

3.2 Fringe sensor requirements and technical constraints

From the above considerations, the following requirements on unit level can be compiled for DARWIN science beam metrology:

Sensor Actuator	requirement	value	comment
Fine Pointing Tip/Tilt Metrology, absolute and relative	Readout frequency	10Hz	Relative beam pointing
	Range	6000" half cone on 10mm beam	To cover initial bias and mounting errors
	Noise	< 3200 mas (RMS) on 10mm beam	Equivalent to 1000 mas/√Hz @ 10Hz
	Bias and mounting error(1)	1400 mas (3σ) on 10mm beam	All scaled from 200mm to 10 mm beam
Fringe Sensor (3)	Readout frequency	50Hz	OPD
	Range (coherence length)	4µm	In acquisition, locking, and fine control.
	Maximum OPD drift	8.5µm/s	
	Noise	0.5nm RMS	Intermediate star case (mv=9)
	Bias	-	Not observable at GNC level
Optical Delay Lines	Command rate	50Hz	
	Range	+/- 1 cm	For fringe acquisition
	Stability	0.7 nm RMS	Around the ODL zero position.
	Response time – Position control	< 20 ms	Staircase profile for fringe acquisition with 100ms step
	Quantification – Position control	~10nm	Not critical only used for fringe acquisition
	Response time – Velocity control	< 2 ms	For tracking mode (compatibility with control rate)
	Quantification – Position control	1nm/s	
Tip/tilt mirrors	Command rate	10Hz	
	Range	+/- 600"	

Astrium GmbH
88039 Friedrichshafen
Telephone: (07545) 800
Telefax: (07545) 84411

Sensor Actuator	requirement	value	comment
	Stability	<500 mas RMS	Scaled from 200 mm to 10 mm
	Response time	< 100 ms	
	Quantification	2000mas	
FEEPs	Command rate	1Hz	
	Range	0 – 3 mN	Max thrust defined by manoeuvres capability
	Noise	< 2 µN/√Hz	Per axes, including thrust amplitude and thrust direction stability.
	Quantification	1µN	
	Minimum thrust	1µN	
	Response time	100ms	

(1) All biases and mounting errors are to be understood "after calibration and commissioning phase".

(2) Fringe Sensor is driving the system so these are not recommendations, but hypotheses on which design is made

Tab. 3-7 Synthesis of unit requirements for DARWIN science beam metrology

3.2.1 DARWIN photon flux limits

Preliminary sensor performance photon noise limits

Within very simplified optical performance models; fundamental photon-noise limits for DARWIN have been estimated, based on the following boundary conditions

- 35% transmission (worst case, goal 60%) for each of the four 3.5 m telescopes up to the fringe sensor unit
- for OPD as well as for interferometric sensing of relative pointing.
- initial bandwidth allocation for FSU band from 620 to 700 nm, this bandwidth shall be optimized/modified in course of this study
- a cooled silicon CCD with initially negligible dark current and readout noise compared to the DARWIN worst case photon noise is to be underlaid initially, with noise inclusion in later phases of this study.

The underlying idea is that the fundamental photon noise limits are practically implementation-independent as long as identical spectral bandwidth of FSU operation is respected:

The below performance numbers were derived preliminarily and one goal of this study is to consolidate them. They were assessed for the whole range of DARWIN target stars with visible magnitude in V-band (m_v) between 3.32 (brightest star) down to 12 (faint M-dwarf).

Astrium GmbH
88039 Friedrichshafen
Telephone: (07545) 800
Telefax: (07545) 84411

	m_v	OPD RMS @ 10 Hz	Pointing RMS @ 10 Hz	Comments
Brightest star of target catalogue	3.32	0.017 nm	1.4 mas on 10 mm ∅ beam	
Sol at 15 pc	5.65	0.05 nm	4 mas on 10 mm ∅ beam	HIP75181, G2V, 15 pc
Intermediate star	9.0	0.23 nm	19 mas on 10 mm ∅ beam	
Dimmest star	12.0	0.93 nm	76 mas on 10 mm ∅ beam	

Tab. 3-8 Estimated fundamental photon noise limits of DARWIN science beam metrology

Actual photon counts for DARWIN FSU

In terms of quantitative photon fluxes, the above stellar magnitudes account for the below photon counts/second. As starting point, following [Bely2003], we assume for m_v=0 a photon flux of 9.6×10^{10} photons/(m^2 micronbandwidth second) around 550 nm (V-band). Though this is not exactly the foreseen FSU band around 650 nm, we stick to this number for the time being, since the current DARWIN target catalogue only provides this spectral band information in V, not in R-band around 700 nm. For most stars, the error is negligible.

	m_v	Photons/second in 80 nm bandwidth
Brightest star of target catalogue	3.32	1.2×10^9
Sol at 15 pc	5.65	1.4×10^8
Intermediate star	9.0	6.5×10^6
Dimmest star	12.0	4.1×10^5

Tab. 3-9 Photon counts for DARWIN science beam metrology/FSU (per telescope)

Certainly the FSU OPD reconstruction is the most critical element of the overall DARWIN science beam metrology, as can be seen by comparison from table Tab. 3-8 with requirements table Tab. 3-4.

3.2.2 DARWIN closed loop simulation of OPD control and FSU performance

Presently all closed loop simulations of OPD control and FSU performance are done with a “black box” idealized model of the FSU, with parameters selected as of Tab. 3-4. In a more detailed physical modelling of the FSU as to be undertaken in this study it will become obvious that tis ideal behaviour

Astrium GmbH
88039 Friedrichshafen
Telephone: (07545) 800
Telefax: (07545) 84411

cannot be achieved, but that the OPD control algorithms have to be designed sufficiently robust to deal with these non-ideal, but physical sensor response. The understanding of these non-idealities is beyond pure performance assessments the second goal of this activity

Astrium GmbH
88039 Friedrichshafen
Telephone: (07545) 800
Telefax: (07545) 84411

4 Classification and comparison of fringe sensor principles

4.1 Principal classifications

A large variety of fringe sensor designs is principally realizable, and several of these have been already implemented in ground-based stellar interferometer applications.

The main differences are

- Beam combination in pupil plane or image plane
- White light fringe sensor or additional spectral dispersion (dispersed fringes)

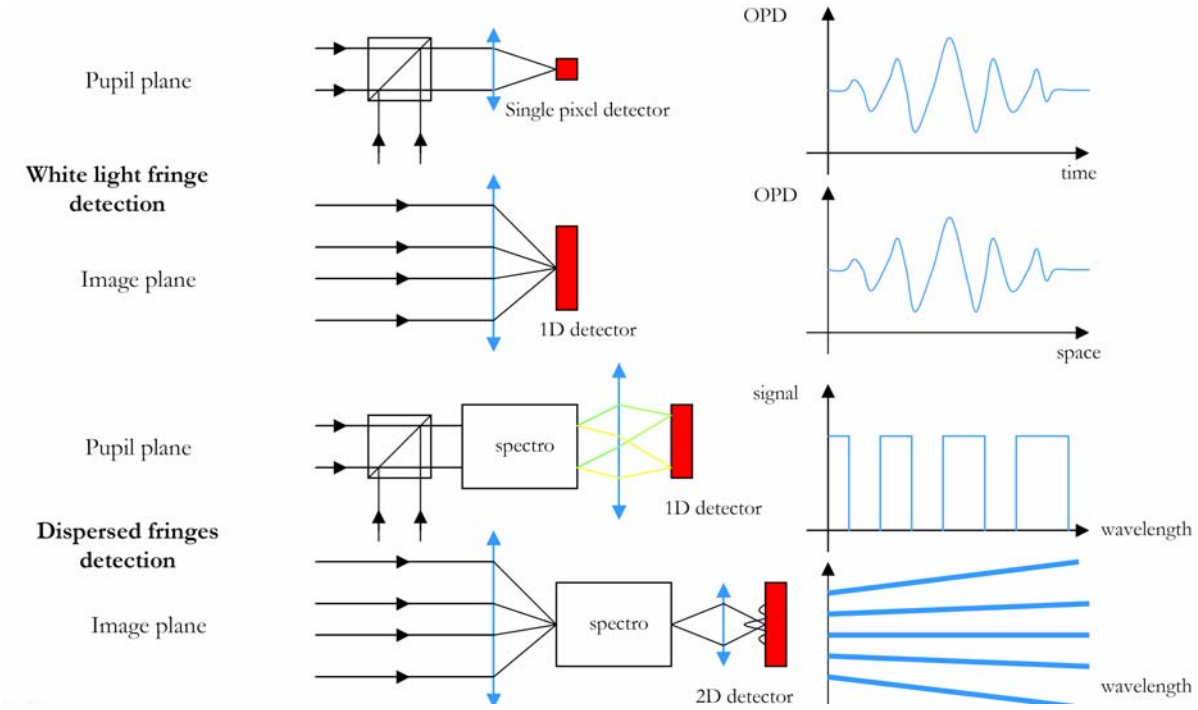

Figure 4.1-1 Visualization of different fringe sensor concepts

A) Pupil plane/ white light fringe sensor

This approach in general requires active scanning of OPD throughout a significant fraction of the coherence length $\lambda^2/\Delta\lambda$ of the fringe packet with central bandwidth λ and spectral bandwidth $\Delta\lambda$. The maximum of the fringe envelope must be determined, defining zero path difference ZPD. This active scanning is highly discouraged for DARWIN applications due to the introduced microvibrations, reaction forces, and the sub-nm stability requirements on the other hand.

If the system is highly stable, once the maximum of the fringe envelope has been identified, it can in principle be tracked statically. To avoid working at a badly defined maximum, an artificial achromatic 90° phase shift can be introduced in the fringe sensor band of one interferometer arm. This extension

Astrium GmbH
88039 Friedrichshafen
Telephone: (07545) 800
Telefax: (07545) 84411

has been successfully implemented in the Astrium MAII Nulling Breadboard. Nevertheless there are major concerns with this DC-readout based approach on achievable critical long-term stability, which must be sub-nm over one week.

Another example for this type of instrument is the PRIMA FSU, which will soon be installed at ESO's VLTI at Chile, Cerro Paranal.

B) Image plane/ white light fringe sensor

Here the incident beams generate a spatially resolved fringe pattern on a CCD camera in an image plane. The envelope of this fringe pattern is given by the Airy disk of each individual beam, and within this Airy disk envelope, fringe patterns form by interferometric superposition, which can be analyzed by Fourier optics techniques.

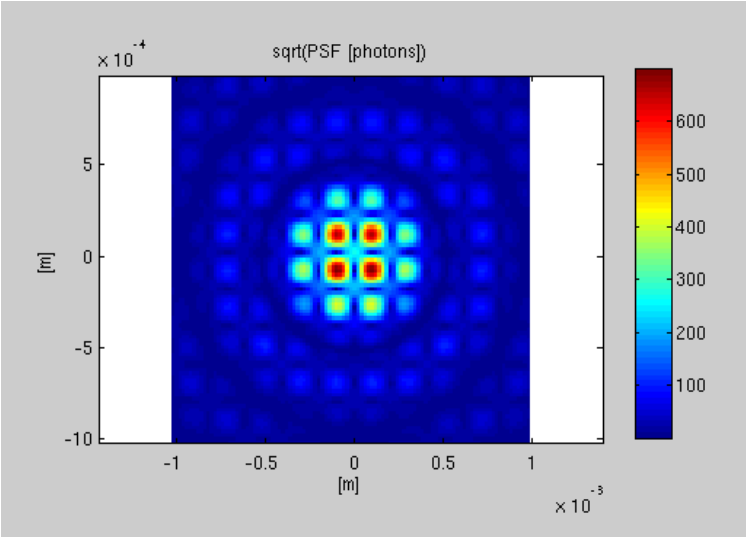

Figure 4.1-2 White light fringe pattern in image plane

This approach is currently baselined to be used as DARWIN fringe sensor. A breadboard has been developed (dubbed "DWARF") within an ESA TRP activity. The working principle of DWARF relies on a two-dimensional arrangement of the (three) incoming beams and multi-axial imaging onto a CCD focal plane.

The main advantage of this approach consists in that it allows for combining the FSU functionality with integrated sensing of tip/tilt and of higher-order Zernike modes.

The LBTI fringe tracker relies on this principle, too, but with order of magnitude relaxed requirements on OPD performance.

C) Pupil plane/ dispersed fringes fringe sensor

This is basically approach A with the overall bandwidth being subdivided into multiple subbands of bandwidth $\Delta\lambda_{sub}$.

The advantages are:

- Significantly longer coherence lengths $\lambda^2/\Delta\lambda_{sub}$

Astrium GmbH
88039 Friedrichshafen
Telephone: (07545) 800
Telefax: (07545) 84411

- Active scanning of OPD can be avoided since due to the multiple spectral channel readouts, OPD can be uniquely reconstructed within the overall fringe packet.

A candidate instrument is the MIDI instrument from MPIA Heidelberg at ESO VLTI at Cerro Paranal.

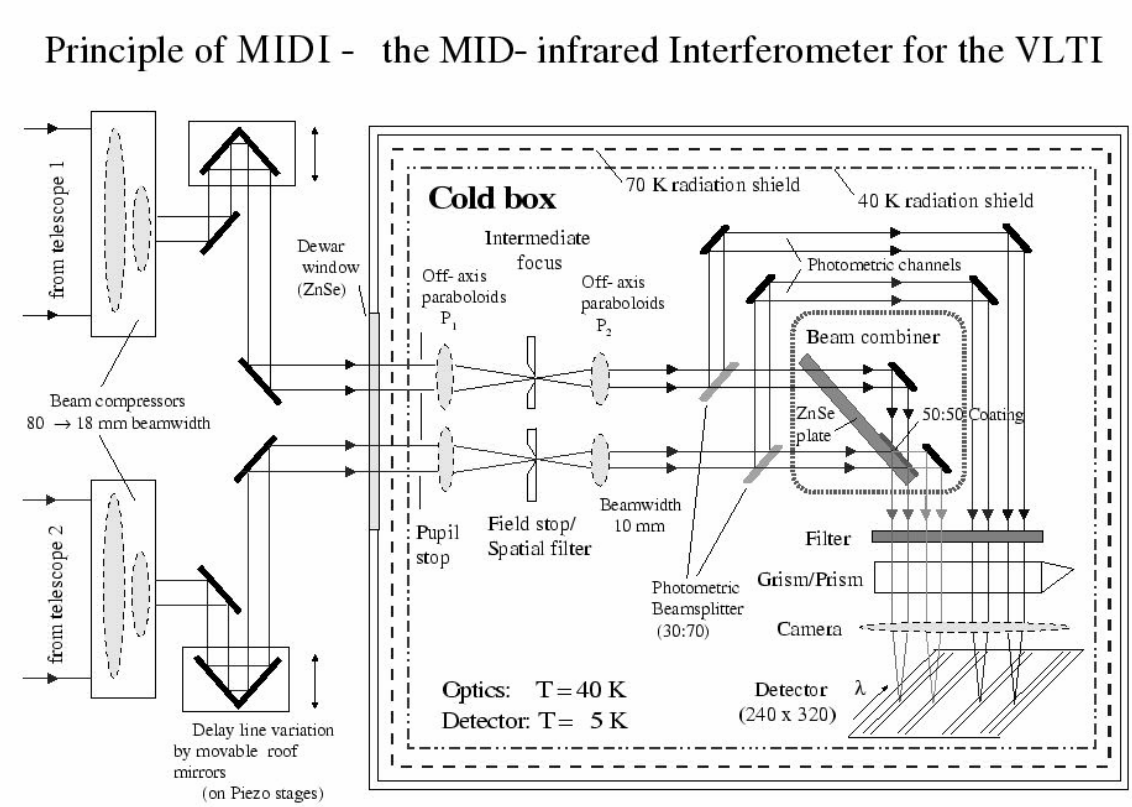

Figure 4.1-3 MIDI beam combiner (source: ESO/MPIA Heidelberg)

The main disadvantages are that fringe pattern intensities have to be measured absolute, and therefore a high sensitivity of fringe sensor readout to sensitivity drifts of individual photo detectors/ CCD pixels exists. Of then this sensitivity is recalibrated through an active mechanical scan of OPD through the fringe sensor operating range. For DARWIN application such a mechanical scan is very disadvantageous due to additional mechanical microvibrations introduced.

D) Image plane/ dispersed fringes fringe sensor

Whereas approach B provides a two-dimensional fringe pattern to be analyzed, in this approach the beams are arranged one-dimensionally with non-redundant baselines, providing a one-dimensional fringe pattern, and are dispersed in the orthogonal direction. The typical instrument for this approach is AMBER at VLTI.

AMBER uses image plane combination of three beams, with non-redundant 1D baseline. Dispersion is superimposed in the perpendicular direction (dispersed fringes).

Due to the fringe dispersion, a wider spectral bandwidth can be used here than in the white-light approaches in the image plane approach, resulting in higher SNR.

Astrium GmbH
88039 Friedrichshafen
Telephone: (07545) 800
Telefax: (07545) 84411

Nevertheless a long coherence length $\lambda^2/\Delta\lambda_{sub}$ >= 100λ is provided for fringe acquisition in the individual spectral subbands.

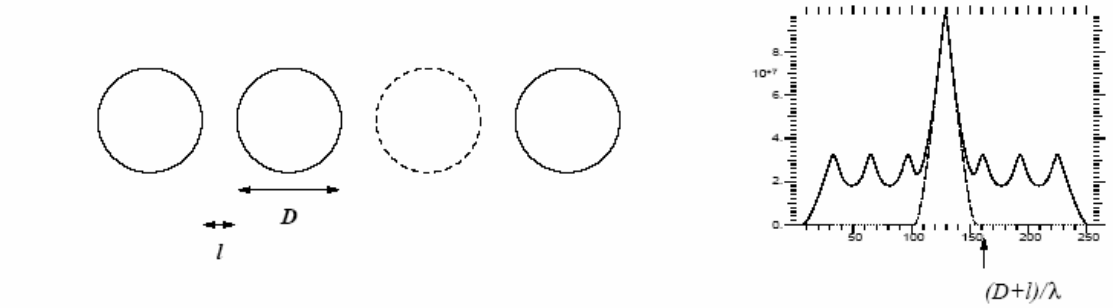

Figure 4.1-4 Left: the beams have a diameter of 20 mm and are separated by 5 mm. Right in Fourier space, the fringe peaks are located respectively at 25mm/λ, 2x25mm/λ, and 3x25mm/λ. [AMBER99]

Image Plane at ZPD for a single wavelength

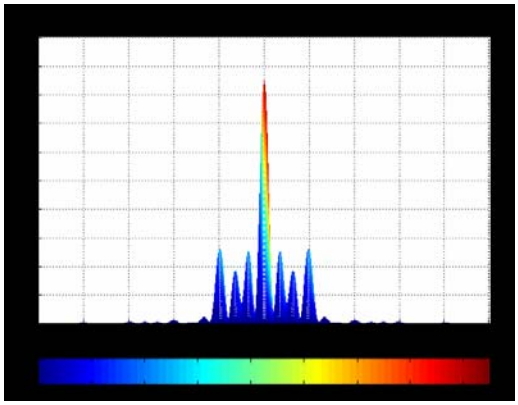

Image Plane with 180° phase offset imposed on beam 2, for a single wavelength

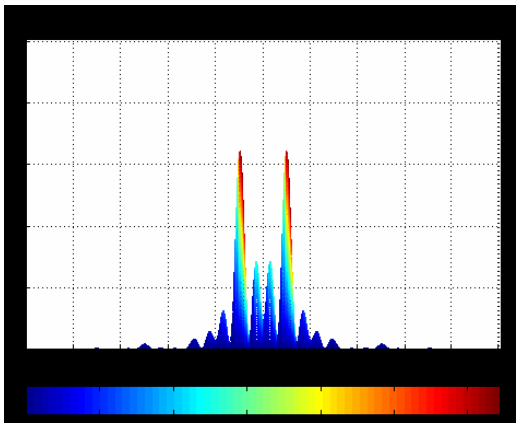

Figure 4.1-5 Influence of OPD on fringe pattern on FSU detector array

Astrium GmbH
88039 Friedrichshafen
Telephone: (07545) 800
Telefax: (07545) 84411

4.2 Trade

Comparing these different approaches, we end up with the below coarse decision matrix.

	A *PRIMA*	*B* *DWARF*	*C* *MIDI*	*D* *AMBER*
Resolution	**+**	**+**	**+**	**+**
Longterm Stability	**-**	**+**	**+**	**+**
Tip/Tilt Sensing	**-**	**+**	**-**	**-**
Aberration Sensing	**-**	**+**	**-**	**-**
Broadband	**+**	**-**	**+**	**+**
Acquisition/ ***Coherence length***	***0***	***0***	**+**	**+**
Passiveness	**-**	**+**	**+**	**+**

Tab. 4-1 Qualitative comparison of different FSU concepts. (**+** means advantageous, **0** is indifferent, **-** means disadvantageous)

Obviously there is no clear favourite from this qualitative decision matrix, therefore we have to thoroughly study all implementation details.

4.3 Selection of candidate fringe sensor principles for DARWIN

The following two candidate fringe sensor principles have been preselected for further analysis

- Approach B) white light fringe sensor in image plane
- Approach C) dispersed fringes fringe sensor in pupil plane

The reasoning is:

Candidate 1 approach B) "white light fringe sensor in image plane" is the ESA baseline for the DARWIN fringe sensing unit (FSU) DWARF, as detailed in [PDD2005].

Astrium GmbH
88039 Friedrichshafen
Telephone: (07545) 800
Telefax: (07545) 84411

Candidate 2 approach C) "dispersed fringes fringe sensor in pupil plane" is exactly complementary to approach B) in terms of fringe dispersion and pupil plane.

Therefore if those two approaches are analyzed in detail, the main features of approach A) and D) are automatically included, too. Consequently A) and D) can be reassessed/reevaluated once B) and C) have been analysed in detail.

4.4 Description of white light image plane FSU for DARWIN

4.4.1 Calculating the intensity pattern on the CCD

As reference point we choose four beams in a pupil plane in a distance *d* in front of an ideal lens. In general two aperture configurations will be analyzed:

- redundant baselines: Four beams with beam diameter 10 mm located on the corners of a square with 15 mm edges. Here the interferometric baselines, i.e. the vectors from subaperture center to subaperture center are redundant and non-unique
- non-redundant baselines: Here each interferometric baseline is unique in 2D. An example implementation is locating three beams on the corners of an equilateral triangle, and having the fourth beam in the middle.

Figure 4.4-1 Redundant (left) and non-redundant (right) aperture plane beam arrangement

Scalar optics Fraunhofer propagation modelled by Fourier transform

Within a coherent optical system consisting of an ideal lens with focal length *f*, the propagation for an electrical field distribution $E_d(u)$ in a given plane a distance *d* in front of the lens, to the back focal plane of the ideal lens can be described by the following Fourier equation [Goodman] , eq. 5-19:

$$f(x) = \exp(i\frac{2\pi}{\lambda f}(1-\frac{d}{f})x^2)/(i\lambda f) \int E_d(u)\ \exp(-i\frac{2\pi}{\lambda f}ux)\,du$$

The intensity on a CCD in this focal plane is $|f(x)|^2$. Furthermore allocations for photon noise, dark current, and readout-noise per pixel and per readout have to be added.

Astrium GmbH
88039 Friedrichshafen
Telephone: (07545) 800
Telefax: (07545) 84411

4.4.2 OPD reconstruction: Analytic approach for perfect wavefronts

The physical quantity that solely can be measured is a pixel-based intensity distribution on the CCD in the image focal plane. But the phase of the underlying electrical field distributions cannot be measured directly by the CCD. Therefore phase information must be reconstructed.

In a most elementary, analytical approach, the phase distribution is calculated via the so-called optical transfer function.

For an image of a point-source (in principle *only* for a point source!), the intensity measured is related to the incoherent optical transfer function of the system under incoherent illumination, see [Goodman], eq. 6-22. The (inverse) Fourier transform of this intensity pattern is known as the optical transfer function (OTF) of the optical system.

On the other hand, the OTF can analytically be derived from the aperture function F(u,v) through autocorrelation of the aperture function F ([Goodman], eq, 6-28).

Pupil/Aperturefunction $F(u)$		Amplitude PSF $f(x)$
$F(u)$	$\Rightarrow$	$f(x)=\int \exp(i2\pi u\,x)\,F(u)\,du$
$\Downarrow$	FourierTransform	$\Downarrow$
$\Downarrow$ Autocorrelation		$\Downarrow$ Intensity $\lvert..\rvert^2$
$\Downarrow$	InvFourierTransf	$\Downarrow$
$\Phi(u')=\int F^*(u)\,F(u+u')\,du$	$\Leftarrow$	$\lvert f(x)\rvert^2$
$=\int \exp(-i2\pi u'x)\lvert f(x)\rvert^2\,dx$		
Autocorrelation $\Phi(u')$		Intensity PSF $\lvert f(x)\rvert^2$

For perfectly flat wavefronts, this OTF Φ(u') can be analytically calculated as function of different OPDs.

For non-redundant baselines in the aperture function F(u,v), it can be shown that the phase of the autocorrelation side peaks Pxy, which emerge through crosscorrelation of subaperture x and y, equals the phase difference between subaperture x and y

$$Pxy=\varphi_x - \varphi_y$$

A similar approach has been described in [Baron]. Limitations of this approach occur if non-perfect aberrated wavefronts are present on each beam individually, be it due to tip/tilt, defocus or further higher order aberrations.

Though this analysis has been done without noise, a straight-forward extension is possible, described in [Baron], taking into account known noise sources in the system. This leads to a maximum likelihood estimator based on a least squares optimization for OPD, which has significantly better performance if operations close to the photon noise limit are required as in the DARWIN case.

Astrium GmbH
88039 Friedrichshafen
Telephone: (07545) 800
Telefax: (07545) 84411

4.4.3 OPD and tip/tilt reconstruction I: Phase retrieval using Gerchberg-Saxton iteration

Next step towards higher receonstruction robustness and insensitivity to external perturbations is to implement the Gerchberg-Saxton error reduction algorithm which iteratively transforms between image and pupil plane, and modifies the initial estimators continuously. A good summary in provided in [Fienup1982], where also a suitable "squared error criterion" merit function is provided for stop of iteration.

The Gerchberg-Saxton algorithm was originally invented in connection with the problem of reconstructing phase from intensity measurements and consists of the following four simple steps:

(1) Fourier transform an estimate g_k of the object;

(2) replace the modulus of the resulting computed Fourier transform G_k with the measured Fourier modulus F to form an estimate of the Fourier transform;

(3) inverse Fourier transform the estimate G'_k of the Fourier transform; and

(4) replace the modulus of the resulting computed image g'_k with the measured object modulus f to form a new estimate of the object.

In equations this is, for the kth iteration,

$$G_k(u) = \mid G_k(u) \mid \exp[i\phi_k(u)] \coloneqq F[g_k(x)]$$

$$G'_k(u) \coloneqq \mid F(u) \mid \exp[i\phi_k(u)]$$

$$g'_k(x) = \mid g'_k(x) \mid \exp[i\theta'_k(x)] \coloneqq F^{-1}[G'_k(u)]$$

$$g_{k+1}(x) = \mid f(x) \mid \exp[i\theta_{k+1}(x)] \coloneqq \mid f(x) \mid \exp[i\theta'_k(x)]$$

where g_k and G'_k are estimates of f and F, respectively.

Here and throughout this study functions represented by uppercase letters are the Fourier transforms of the functions represented by the corresponding lowercase letters.

Astrium GmbH
88039 Friedrichshafen
Telephone: (07545) 800
Telefax: (07545) 84411

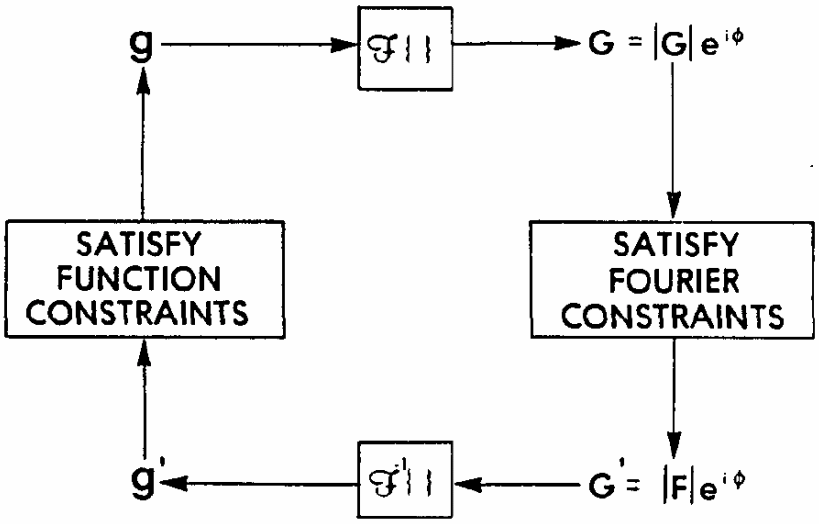

Figure 4.4-2 Visualization of Gerchberg-Sayton algorithm. The "guessed" functions g and its Fourier transform G are iteratively (inverse) Fourier transformed, and after each Fourier transform, the modulus of the guessed function is substituted by actually measured numbers.[Fienup1982]

As depicted in the above picture, the Gerchberg-Saxton algorithm is easily generalized to a large class of problems. The generalized Gerchberg-Saxton algorithm can be used for any problem in which partial constraints (in the form of measured data or information known a priori) are known in each of two domains, usually the object (or image) and Fourier domains. One simply transforms back and forth between the two domains, satisfying the constraints in one before returning to the other. This generalization of the Gerchberg-Saxton algorithm will be referred to as the error-reduction algorithm since, as is shown in [Fienup1982], the error decreases with each iteration.

Though differential OPD and tip/tilt can be unambiguously reconstructed with such an approach, such an approach only provides Zernike magnitude for even Zernikes, not the actual complex Zernike phase.

4.4.4 OPD and tip/tilt reconstruction II: Phase diversity algorithm

The next-to-next step, full phase diversity with gradient search optimization of merit functions, appears very interesting and promising for detailed analysis in a next study phase, especially since faster convergence can be expected here.

The extension consists in measuring intensity data in focus as well as in a deliberately defocused image plane. This so-called "phase diversity" allows for a unique reconstruction of phase for all Zernikes.

The principal approach consists in an n-dimensional parametrisation of the aperture function, and subsequent autocorrelation thereof, providing the system OTF properly parametrized. On the other hand the system OTF can be calculated as inverse Fourier transform of a point source image. A

Astrium GmbH
88039 Friedrichshafen
Telephone: (07545) 800
Telefax: (07545) 84411

suitable merit function now allows for numerical iterative minimisation of this merit function in an n-dimensional parameter space, providing a maximum likelihood estimator for the n parameters.

An initial implementation of this kind of algorithms is shortly discussed in section 5.2.2.

Astrium GmbH
88039 Friedrichshafen
Telephone: (07545) 800
Telefax: (07545) 84411

4.5 Description of dispersed fringes pupil plane FSU for DARWIN

4.5.1 Optical concept

A simplified optical concept for pupil plane beam combination and for the generation of dispersed fringes is shown in Figure 4.5-1.

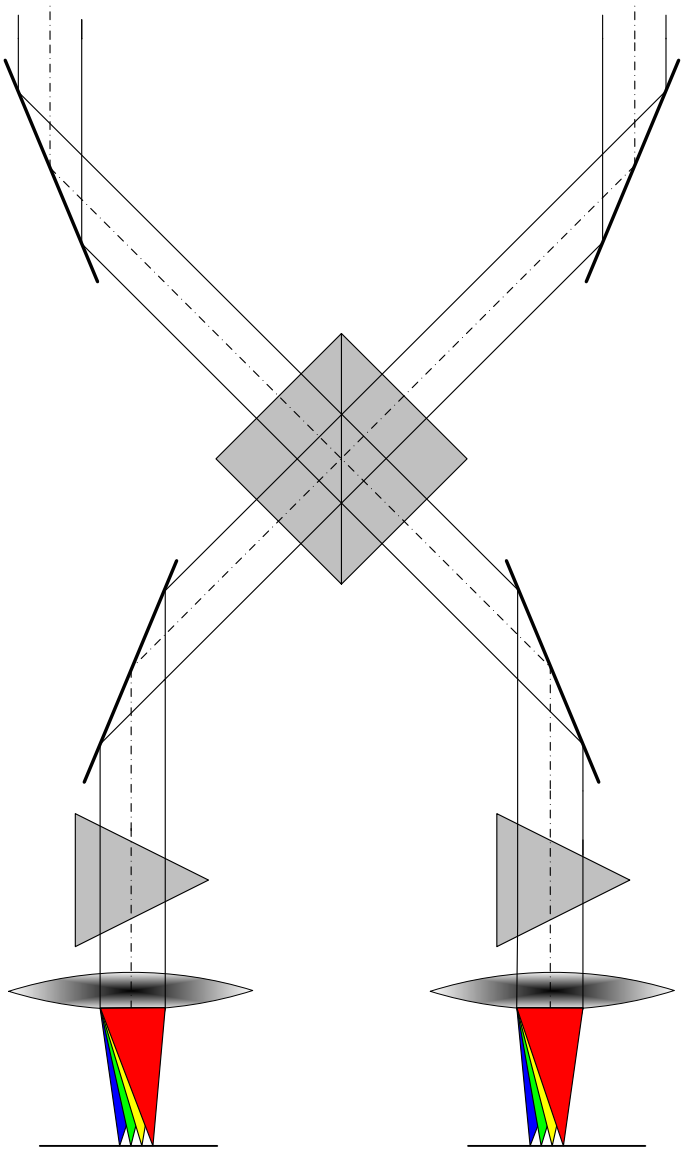

Figure 4.5-1 Conceptual optical setup for pupil plane beam combination and dispersed fringes detection in a stellar interferometer.

Astrium GmbH
88039 Friedrichshafen
Telephone: (07545) 800
Telefax: (07545) 84411

In the conceptual drawing shown above we consider two star light beams. These beams are superimposed in an ideal beam combiner providing π/2 phase shift and 50% reflectance for the reflected beams and vanishing phase shift and 50% transmittance for the transmitted beams. The combined beams exiting the beam combiner are dispersed in a prism each. The dispersed beams leaving the prisms are focused by lenses and finally incident on a one-dimensional detector array each (labelled 'Detector 1' and 'Detector 2' in the above figure). The intensity distribution on the detector arrays is a dispersed Airy pattern. Each pixel of a detector array will collect photons of a particular small wavelength range only owing to the action of the prisms. By summing up the readouts of a group of adjacent pixels the optical power incident within a particular spectral sub-band can be measured. This is schematically visualised in the ensuing figure.

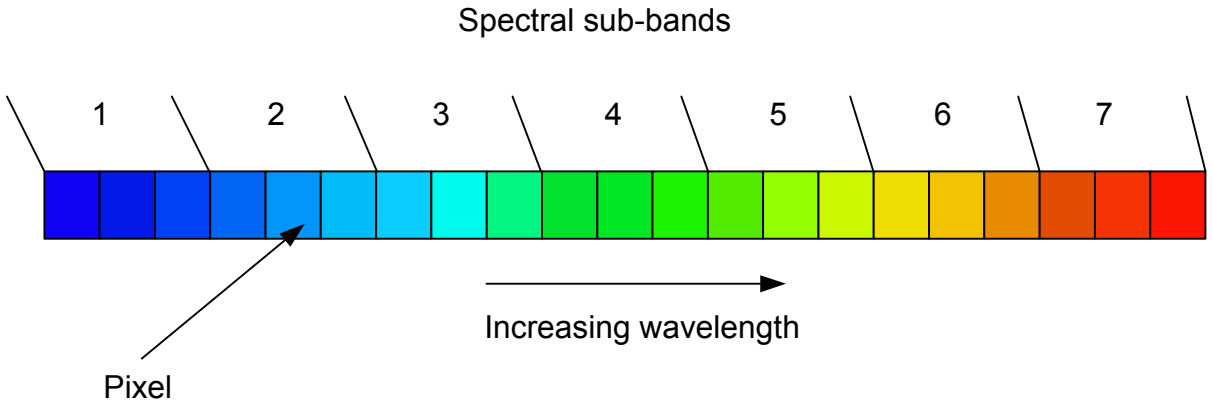

Figure 4.5-2 One-dimensional detector array for measuring the incident optical power within certain spectral sub-bands.

The number of photons collected by a given pixel or by a group of adjacent pixels within a certain time depends on several parameters, in particular on the optical path difference between the two interferometer arms shown in Figure 4.5-1. It is assumed that the two arms receive a planar wavefront from a very distant stellar object. The number of photons incident on the individual pixels can now essentially be predicted based on the generalised Van Cittert-Zernike theorem. We need to know the spectral intensity distribution of the source, its spatial intensity distribution and the optical path difference along the two interferometer arms to the source points on the stellar object.

Fortunately, the stars of relevance for DARWIN are not resolved by the telescopes on-board the collector spacecraft. Therefore they can be considered as unresolved point sources with a unity source visibility. Furthermore the broadband spectral intensity of the source can in general be approximated by piecewise constant narrow sub-bands. For such a sub-band the intensity incident on two corresponding pixels in Detector 1 and 2 as a function of the optical path difference in the two arms is depicted in Figure 4.5-3.

The intensities on the two detectors show a modulated sinusoidal variation ("fringes") as a function of optical path difference and are obviously mirror images of one another: if the pixel on Detector 1 is at its constructive maximum then the corresponding pixel on Detector 2 is at its destructive minimum and vice versa. The sinusoidal period equals precisely the center wavelength λ of the sub-band.

Astrium GmbH
88039 Friedrichshafen
Telephone: (07545) 800
Telefax: (07545) 84411

Knowing the relation between intensity and OPD one could reconstruct the OPD, provided it remains in the range [-λ/4,+ λ/4] and provided that the spectral intensity of the source be known. The latter constraint can be bypassed by forming a dimensionless fringe signal from the energy-proportional readings E1, E2 of our two pixels:

$$f = \frac{E_1 - E_2}{E_1 + E_2}$$

This signal is now limited to the range [-1,+1] as can be seen from Figure 4.5-4. Moreover it passes zero and features a nice steep slope for zero OPD. This is desirable for OPD control around zero OPD.

The combination of fringe signals of different sub-bands belonging to the same optical path difference can be considered a vector, the fringe vector. Based on a fringe vector determined from the pixel readings of the two detectors, the corresponding OPD can be determined using a dedicated look-up table. This look-up table contains fringe vectors versus OPD. The look-up table is then simply searched for the fringe vector being closest to the measured fringe vector.

For the fringe vectors as described above also other methods of normalisation are worth considering. A promising alternative fringe vector normalisation is based on their conversion into unit vectors. With this normalisation the absolute length (norm) of the fringe vectors is not used for table look-up but only the relative sizes of the vector components matter. This normalisation offers benefits in cases of reduced fringe contrast, e.g. due to intensity mismatch between the two interferometer arms.

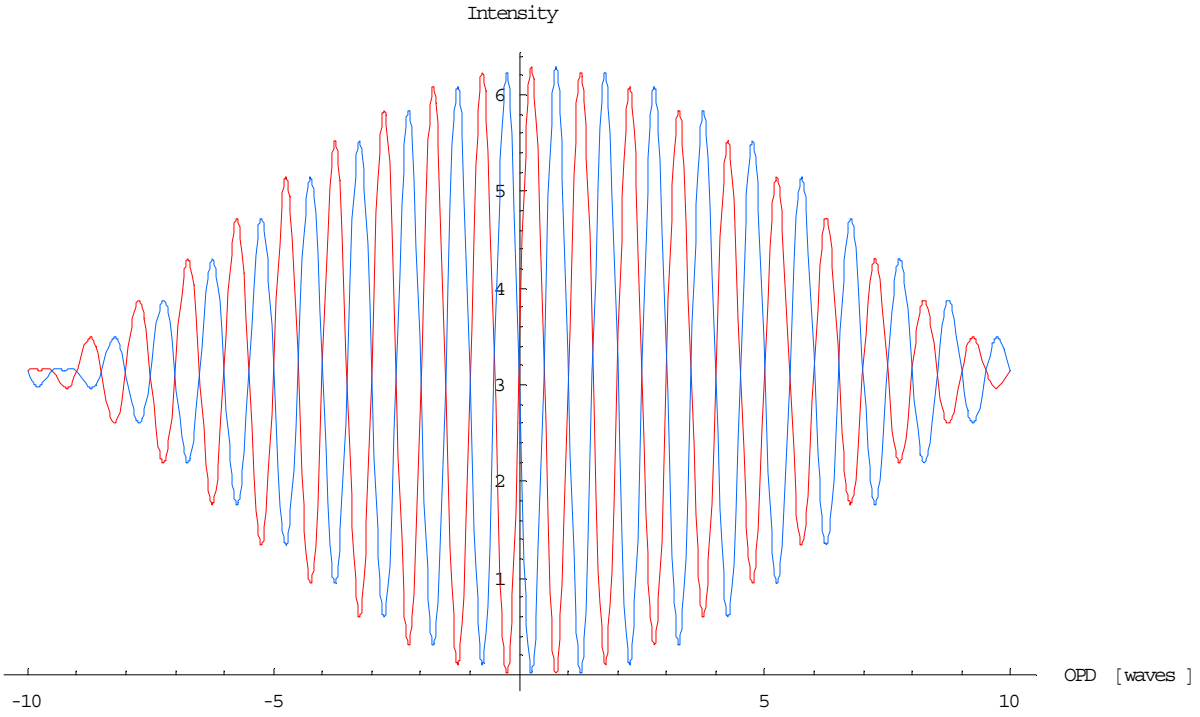

Figure 4.5-3 Pixel intensity on Detector 1 and 2 versus optical path difference. The bandwidth Δλ is λ/10.

Astrium GmbH
88039 Friedrichshafen
Telephone: (07545) 800
Telefax: (07545) 84411

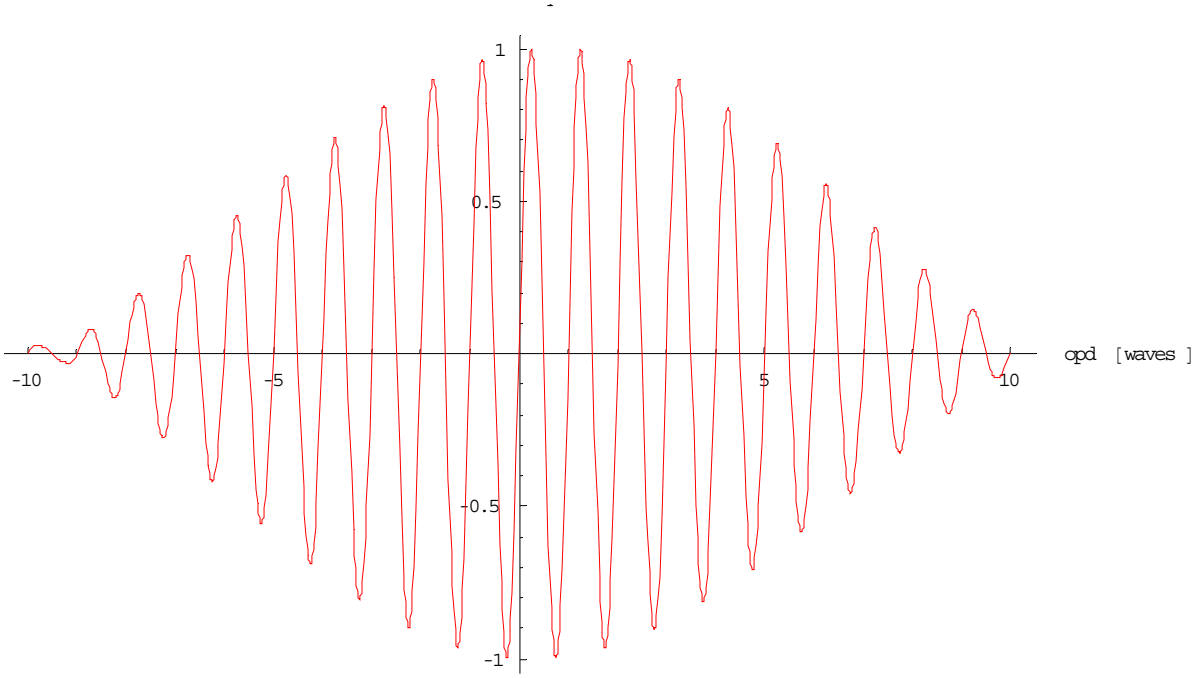

Figure 4.5-4 Normalised fringe signal corresponding to the preceding figure.

4.5.2 OPD reconstruction concept

We have seen in the preceding section how a single pair of detector pixels is in principle sufficient to reconstruct the OPD based on a fringe signal for OPDs not exceeding ±λ/4. This fact has been successfully exploited in Astrium's DARWIN-related Nulling Interferometer Breadboard.

It is now straightforward to extend the OPD range within which a reconstruction of the OPD from measured fringe signals is possible: We need several uncorrelated fringe signals into which the OPD is unambiguously encoded. These signals can be gained by combining the pixel readings of the two detectors in an intelligent way such as to obtain fringe signals having all approximately the same coherence length $\lambda 2/\Delta\lambda$. Such signals are exemplified in Figure 4.5-5.

Astrium GmbH
88039 Friedrichshafen
Telephone: (07545) 800
Telefax: (07545) 84411

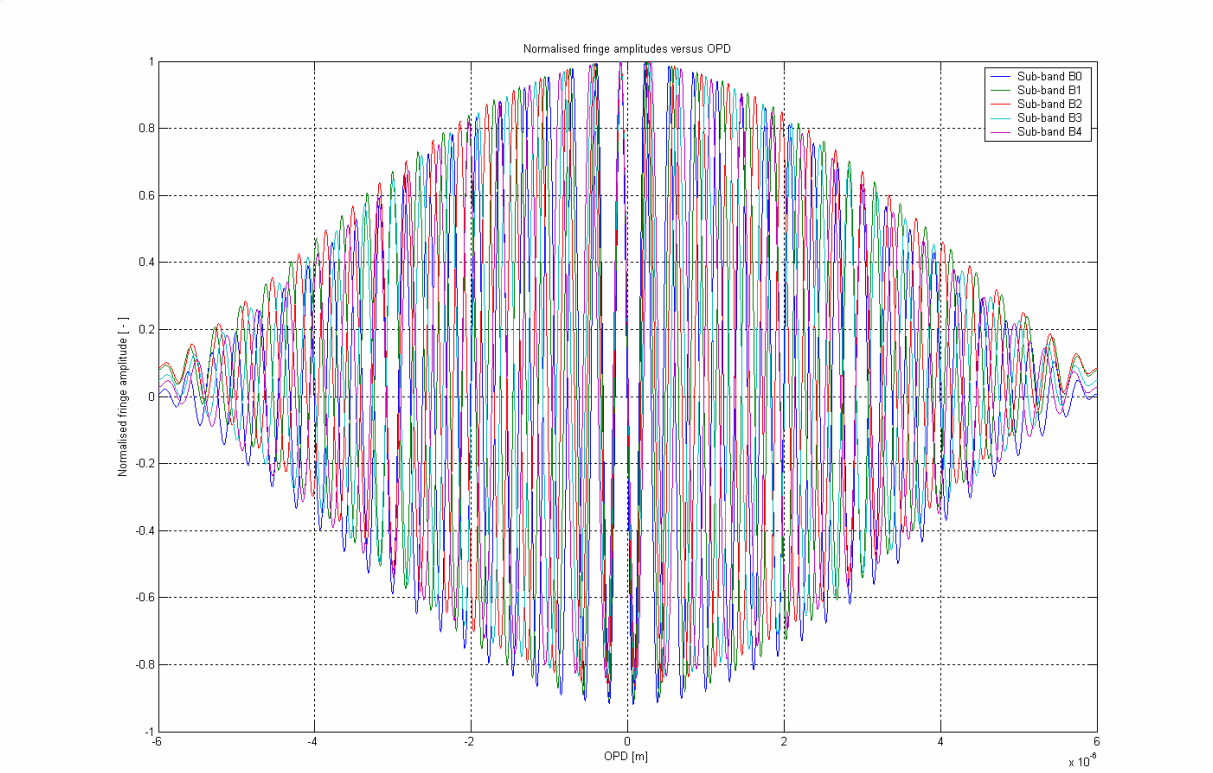

Figure 4.5-5 Fringe signals for five different spectral sub-bands adjusted so as to have all the same coherence length.

4.5.3 OPD reconstruction for DARWIN

For DARWIN we have not only two star light beams between which the OPD needs to be measured but four. This yields six optical path differences two of which are redundant and if measured can be used to check the validity of the measurements. So in case all six OPDs shall be measured for DARWIN six instances of the optical setup shown in Figure 4.5-1 would be required.

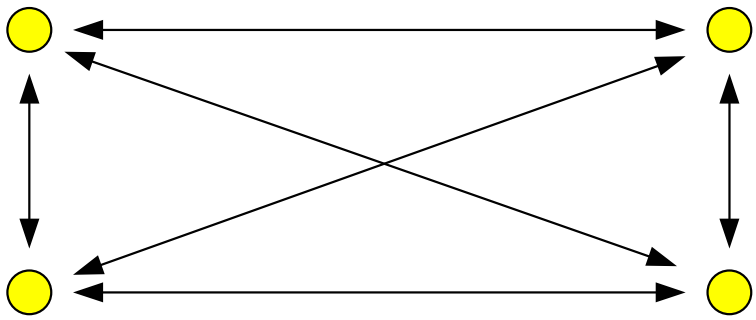

Figure 4.5-6 The four DARWIN star light beams and their pairwise optical path differences.

Astrium GmbH
88039 Friedrichshafen
Telephone: (07545) 800
Telefax: (07545) 84411

5 Analysis of selected fringe sensor principles

With the current understanding of FSU performance and limitations, several critical points have been identified and a simulation campaign has been undertaken accordingly for all discussed fringe sensor designs and algorithms.

5.1 Definition of simulation test campaign

5.1.1 OPD repeatability as function of photon noise

OPD RMS has to be calculated as function of photon noise. The photon fluxes for DARWIN target stars are defined in Tab. 3-9 per individual collector telescope, so in total the photon fluxes are four times higher. Per 80 nm bandwidth, this corresponds to photon counts from 37000 to 96 106 per detector frame readout.

According to Poisson statistics the standard deviation of photon counts is the square root of photon counts, and appropriate Monte-Carlo random simulations have been undertaken, providing OPD RMS as function of photon counts.

This is done at the nominal position with OPD =0, and should be repeated at OPD = λ/4.

5.1.2 OPD linearity throughout FSU working range

OPD is to be scanned from - 5 to + 5 µm according to the presumed working range of +- 4 µm of the FSU as of Tab. 3-7.

5.1.3 Crosstalk of aberrations on OPD accuracy

Now the crosstalk of further beam aberrations beyond piston/OPD is quantified for representative static and dynamic tip/tilt, and lateral beam displacement errors. The respective numbers for RMS and static bias are provided in Tab. 3-2 , scaled to 10 mm beam, and supplemented by DARWIN representative higher order aberrations.

	Values
Tip/tilt (on 10mm beam)	RMS :1.4 arcseconds Bias : 1.4 arcseconds
Lateral beam displacement (on 10 mm beam)	RMS :0.175 mm Bias: 0.125 mm
Defocus, Coma, Astigmatism, Trefoil, Spherical aberration	Bias: 20 nm wavefront error RMS each

Tab. 5-1 Further beam imperfections leading to crosstalk on OPD reconstruction

Astrium GmbH
88039 Friedrichshafen
Telephone: (07545) 800
Telefax: (07545) 84411

5.1.4 Iterative performance improvement

It is expected that the fringe sensor performance will be ideal at the nominal working point of zero OPD. It therefore appears possible to finally achieve λ/1000 OPD error by starting with a significant OPD error, say λ/2, and subsequently correct the actual OPD error with reconstructed OPD values.

5.1.5 Fringe smearing

If throughout the integration time of 20 ms per frame readout (i.e. 50 Hz) the OPD is varying significantly (of order > λ/100), then the fringe pattern is smeared out, looses contrast, and the reconstructed OPD is some kind of average OPD and is erroneous.

Currently OPD velocity is limited to 170 nm = λ/4 per 20 ms frame for fringe acquisition purposes, but only respecting fringe pattern detection. For higher accuracy of OPD reconstruction, this OPD velocity requirement certainly has to be tightened.

5.1.6 Influence of polychromacy on phase retrieval from image plane

There is a certain trade to be analyzed with respect to spectral bandwidth of the fringe sensor. Especially in the image-plane beam combination approach,

- larger bandwidth leads to more photons, which is advantageous,
- but also to contrast loss due to reduced coherence length.

An optimum has to be found for image-plane beam combination fringe sensor units.

Astrium GmbH
88039 Friedrichshafen
Telephone: (07545) 800
Telefax: (07545) 84411

5.2 Phase retrieval based algorithms

5.2.1 Simulation model

The fringe combiner is modelled using a Fourier optics approach as outlined in sect. 4.4.1. In order to take into account defocus effects between aperture/pupil plane, focussing lens and focal plane, a Fresnel diffraction approach has been used according to [Goodman]. Two array configurations have been implemented: a redundant array and a non redundant array as shown in Figure 5.2-1 below.

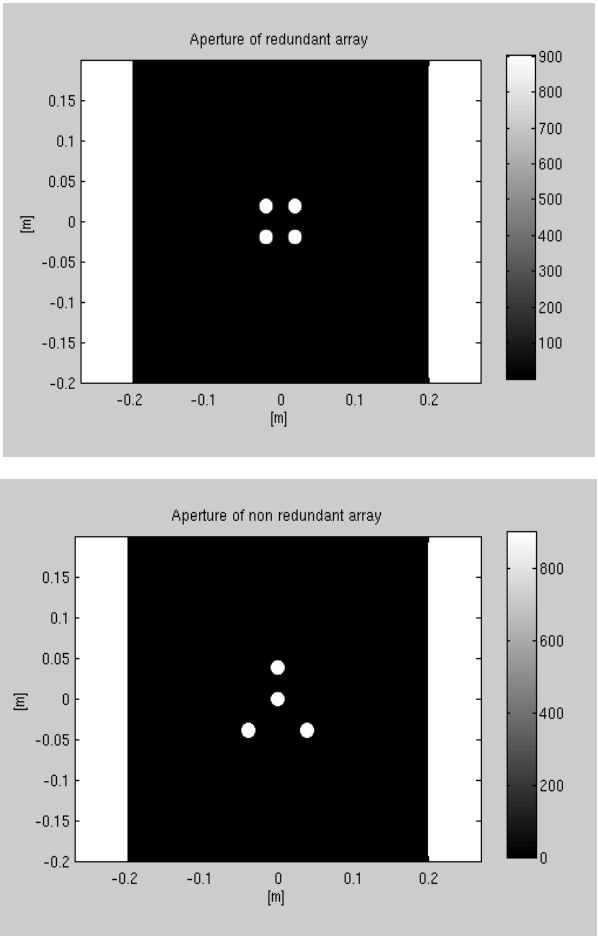

Figure 5.2-1 Apertures / pupil planes for redundant (above) and non redundant array

In order to limit the computing effort, the aperture has been sampled with 512×512 pixels. Since this limits the resolution somewhat, the diameter of a single aperture has been increased by a factor of 2 to 20mm. The wavefront tilt and displacement specifications given in previous sections have been scaled accordingly.

Astrium GmbH
88039 Friedrichshafen
Telephone: (07545) 800
Telefax: (07545) 84411

The wavefront disturbances of the pupil plane have been simulated using Zernike polynomials, which have been scaled to peak to valley values. For RMS wavefront specifications, these values have been rescaled accordingly for each disturbance. The numbering of the Zernikes used is shown below in the Figure 5.2-2 for the first 16 polynomials. Piston is given by Z_0, tilt by Z_1 and Z_2, defocus by Z_4, coma by Z_7 and Z_8, spherical aberration by Z_{12} and trefoil by Z_6 and Z_9.

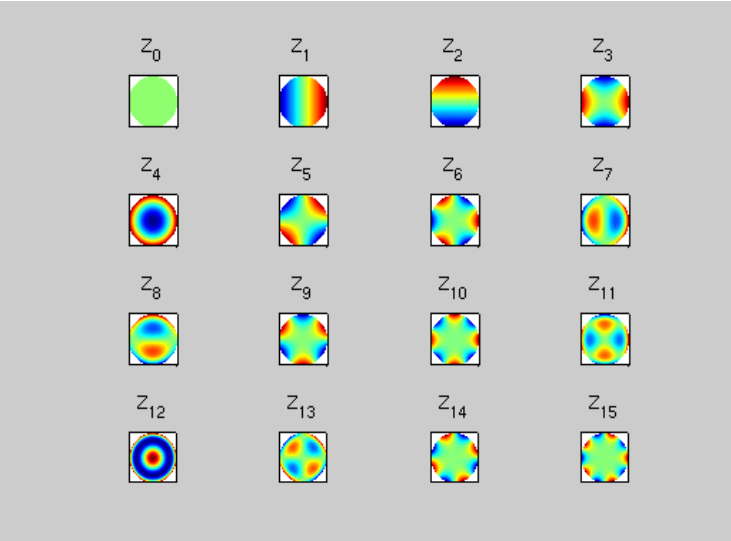

Figure 5.2-2 Numbering scheme used for the first 16 Zernike wavefront disturbances

Some difficulties have been encountered computing the phase of the focal plane fringes via a fast Fourier transform (FFT). These problems have been resolved using a windowing or mask function with smoothed edges as shown in Figure 5.2-3 below. This approach can be seen as a two dimensional equivalent for the windowing functions used in one dimensional signal analysis.

The focal plane intensity distribution and phase of a point source (bright star) for both arrays is shown in Figure 5.2-4 and the phase distributions in Figure 5.2-5. In both figures the nominal case is shown without any aberrations present and for a mean wavelength of 660nm. The focal length has been adjusted to achieve a pixel size of 20µm in the focal plane. That means, the center peak is sampled with 10x10 pixels in case in the redundant array and 5x5 pixels in case of the non redundant array. The difference is caused by the fact that an equal separation between the sub-apertures has been maintained in both configurations, resulting in a larger overall constellation diameter and hence a higher resolution in case of the non redundant array.

Astrium GmbH
88039 Friedrichshafen
Telephone: (07545) 800
Telefax: (07545) 84411

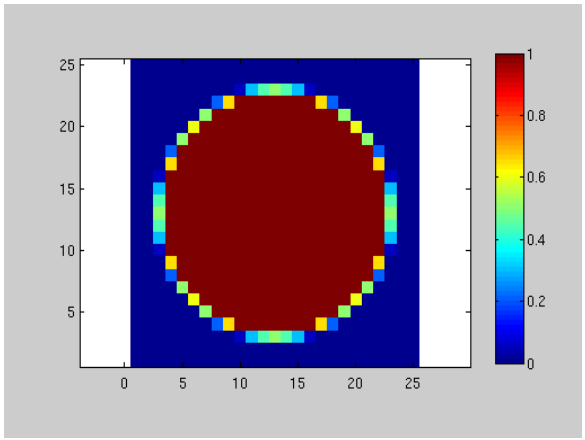

Figure 5.2-3 Smoothed window / mask function

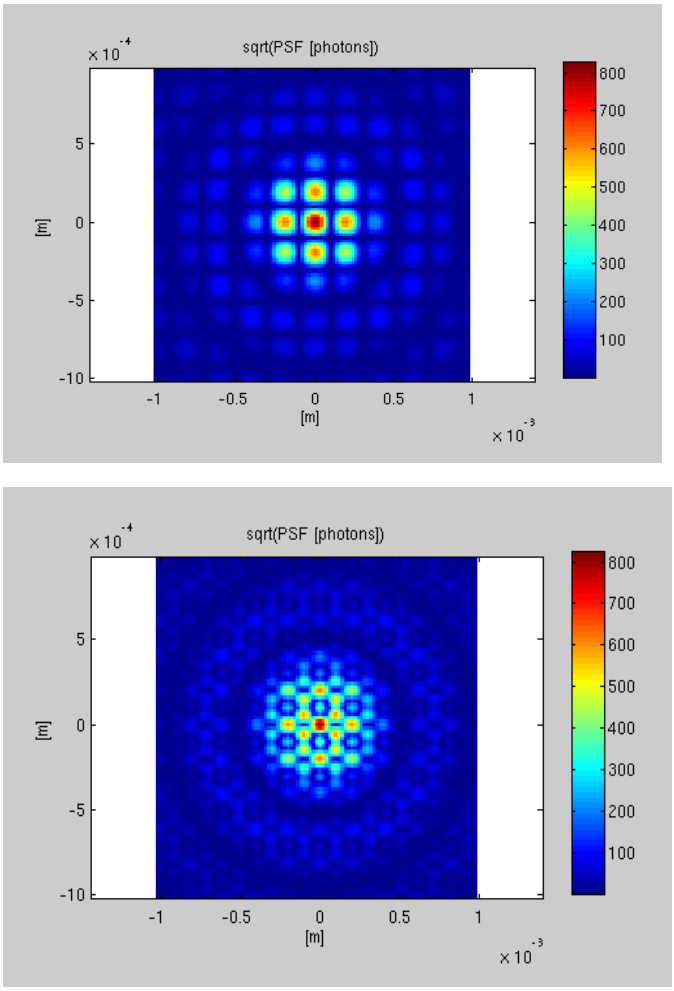

Figure 5.2-4 Focal plane intensity distribution for redundant (above) and non redundant arrays

Astrium GmbH
88039 Friedrichshafen
Telephone: (07545) 800
Telefax: (07545) 84411

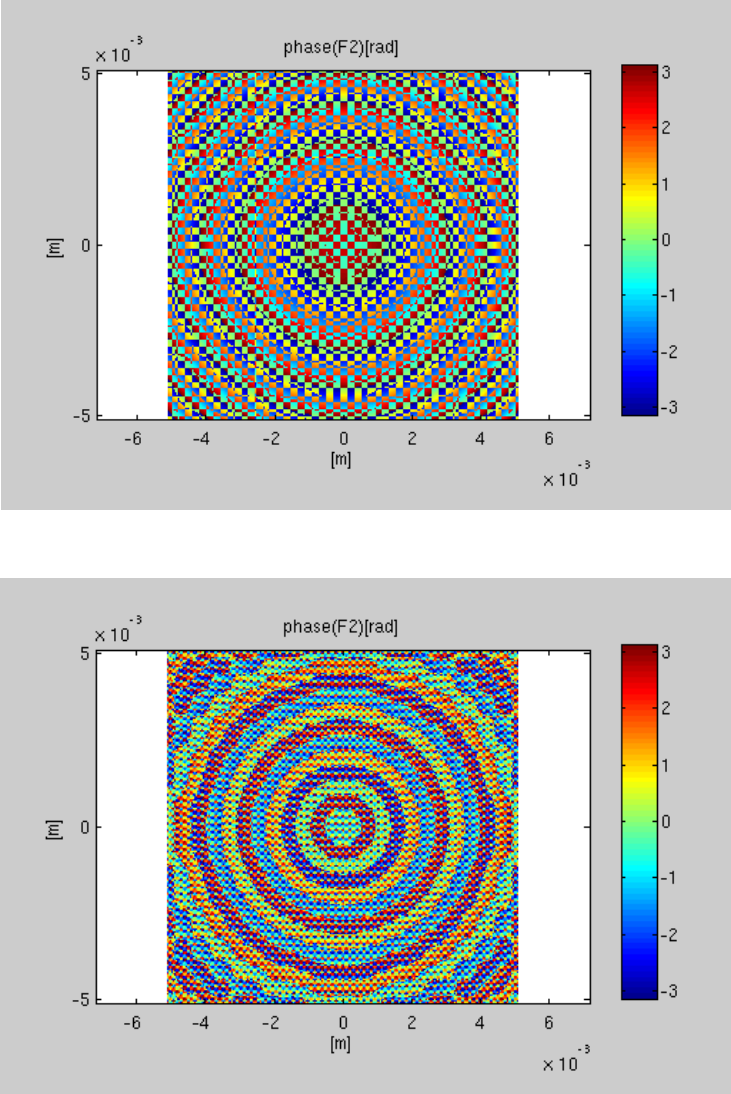

Figure 5.2-5 Focal plane phase distribution in rad for redundant (above) and for non-redundant array

For comparison reasons the results for a pure random piston wavefront error are shown in Figure 5.2-6 for the redundant array. The piston is given by a normal distribution scaled by a mean value of λ/4 RMS. In the present case the central spot has vanished and nearly all the energy is located in the spots next to the central peak. Nevertheless, the image has maintained its original symmetry. The image becomes more confused in the case of a random tilt disturbance as shown in Figure 5.2-7.

The measurement bandwidth of λ = 620 - 700nm has been approximated by 9 discrete frequencies. The resulting focal plane fields have been added incoherently, i.e. the related intensities have been

Astrium GmbH
88039 Friedrichshafen
Telephone: (07545) 800
Telefax: (07545) 84411

combined using a cubic two dimensional interpolation. A linear interpolation has caused significant phase errors of the calculated focal plane images. A random initial phase has been used for each wavelength. The field amplitudes for each frequency have been weighted with appropriate amplitudes obtained from the sun spectrum (T = 5500 K). A comparison of the intensity distribution computed for the whole bandwidth and for the mean frequency of 660nm is shown in Figure 5.2-8. Close to the center only minor differences between the two curves can be observed.

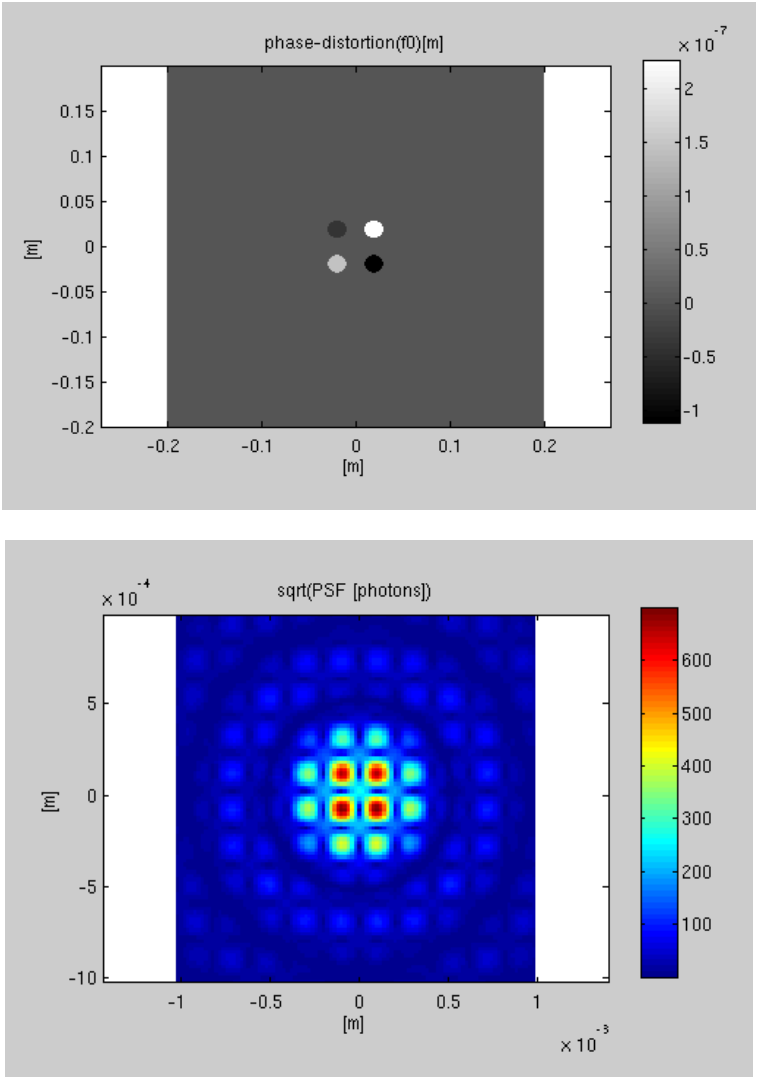

Figure 5.2-6 Random piston wavefront disturbance (aperture plane above and focal plane)

The impact of these disturbances and of other effects on the accuracy of the fringe sensor algorithms will be discussed in the subsequent sections.

Astrium GmbH
88039 Friedrichshafen
Telephone: (07545) 800
Telefax: (07545) 84411

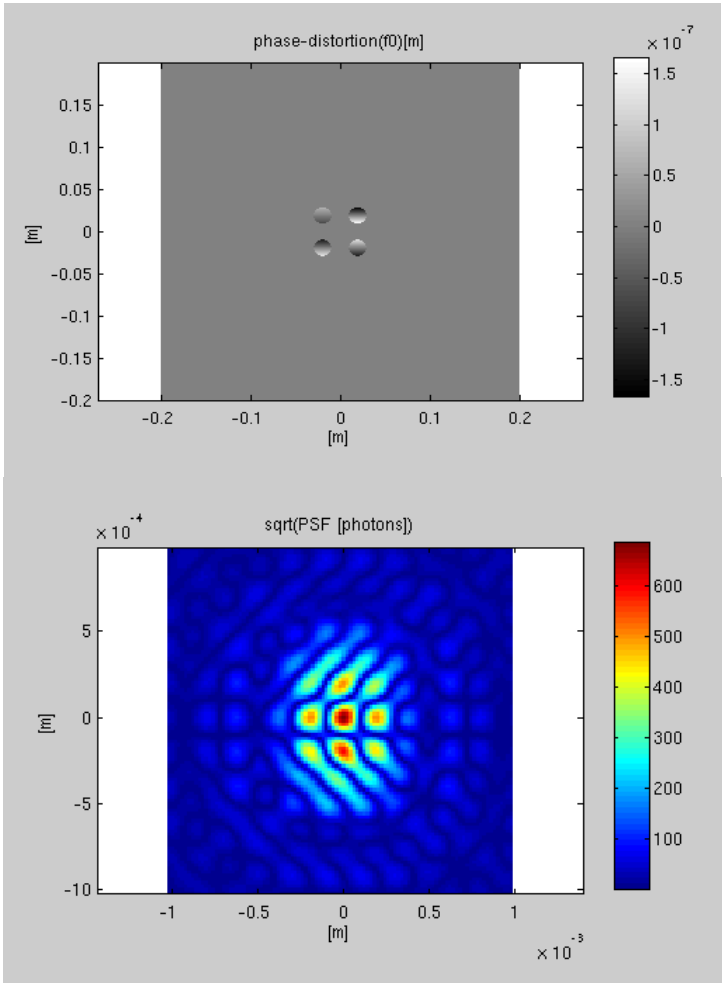

Figure 5.2-7 Random piston aberration (aperture plane above and focal plane)

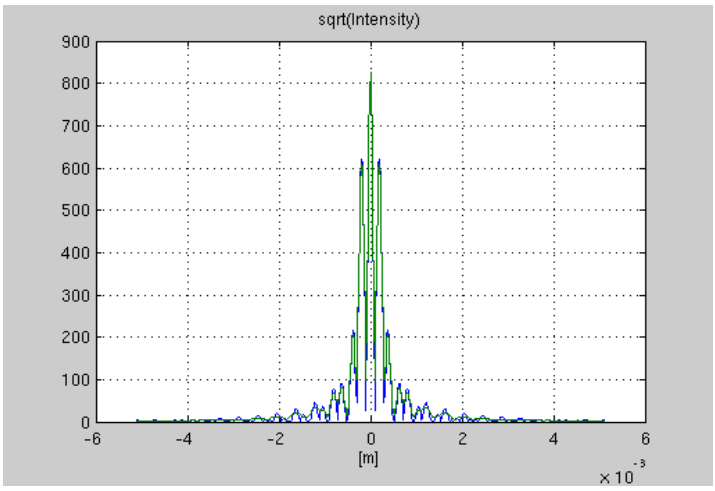

Figure 5.2-8 Cross-section of focal plane intensities obtained at the mean frequency (blue) and the approximated spectrum from 620 to 700nm (green)

Astrium GmbH
88039 Friedrichshafen
Telephone: (07545) 800
Telefax: (07545) 84411

5.2.2 Iterative Algorithms

Gerchberg-Saxton Iteration

The procedure for the Gerchberg-Saxton phase retrieval iteration is described in sect. 4.4.3. The procedure is more or less based on a heuristic approach. It has been shown that the iteration can be interpreted as a special version of a gradient algorithm, i.e. the algorithm can be seen as a prototype for larger class of algorithms and was therefore selected for the implemention. In order to limit the simulation effort, in the present case the Fresnel diffraction approach described above was reduced to Fraunhofer diffraction without amplitude scaling.

The basis features of the iteration can be obtained from the following figures, where the results of a Monte-Carlo simulation are shown for RMS piston values of λ/4 and RMS tilt wavefront errors of λ/20. These values were used to scale normally distributed random numbers. The numbers of iterations have been limited to 20, since in most cases as shown in Figure 5.2-9 the algorithm converges to a constant error level. In all cases 512x512 pixels have been used for image sampling. Using only 256x256 pixels decreases the performance by a factor of approximately ten.

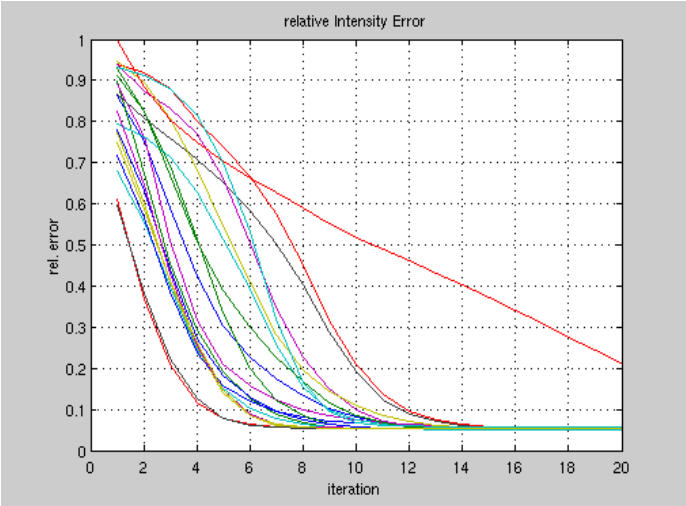

Figure 5.2-9 Relative intensity errors for 20 Monte-Carlo simulation runs and max. 20 iterations per run

The phase retrieval results for a 'lucky shot' are shown in Figure 5.2-10. Due to the exchange procedure between measured (F2) and estimated intensity (G) distribution the intensity error becomes very small after few iterations. In the present case also a very good agreement between simulated (f0) and estimated wavefront phase (ge) has been achieved. From the estimated phase maps the piston errors can be computed after masking of the four aperture images. Taking the mean of the phase arrays and unwrapping the resulting piston phases gives typical errors as shown in the table below, where the values of the fourth row have been subtracted from the set. The results for the Monte-Carlo runs are summarized in Table 5.2-1.

Astrium GmbH
88039 Friedrichshafen
Telephone: (07545) 800
Telefax: (07545) 84411

simulated piston[µm]	estimated piston [µm]	piston error [nm]
0.0687	0.0690	-0.3
0.1924	0.1925	-0.1
0.0107	0.0110	-0.3
0	0	0

Table 5.2-1 Typical piston errors for a (sucessful) Gerchberg-Saxton iteration without noise

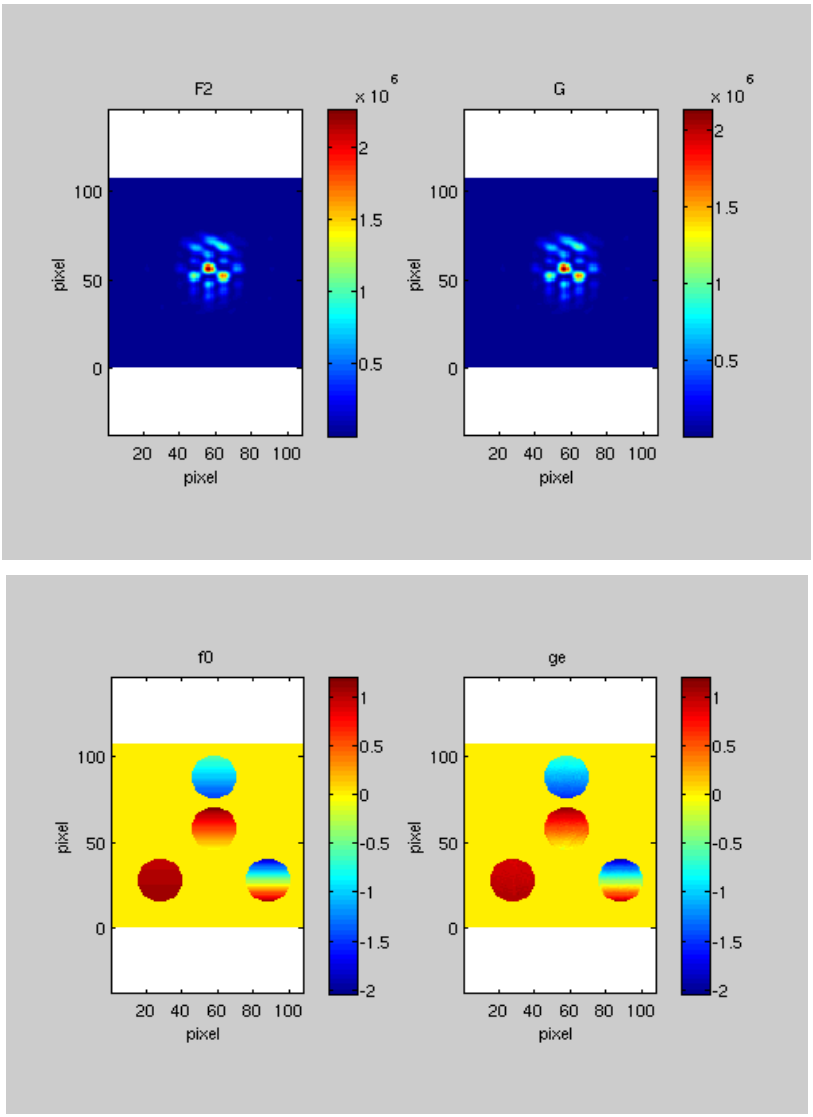

Figure 5.2-10 Measured (F) and estimated intensities (G) and simulated (f0) and estimated (ge) wavefront phase errors

Astrium GmbH
88039 Friedrichshafen
Telephone: (07545) 800
Telefax: (07545) 84411

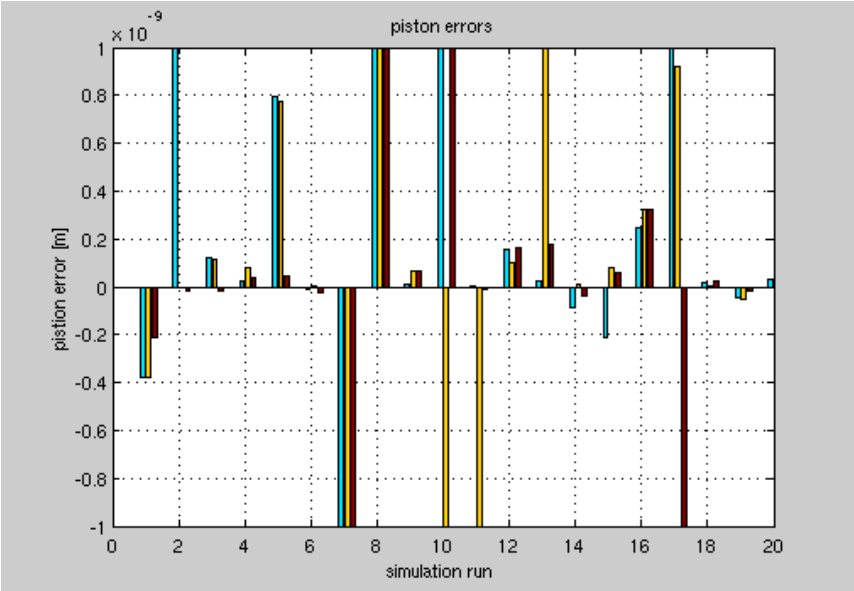

Figure 5.2-11 Piston errors for 20 Monte-Carlo runs without noise (plot is limited to +-1nm)

All values reaching +-1nm indicate that the phase did not converge even though the intensity error has reached steady state conditions (see Figure 5.2-9). With other words, there is no guarantee for a convergence within a limited number of iterations. In special cases even an increased number of iterations may not improve the situation. One reason may be given by phase wrapping effects, which might be removed by suitable advanced unwrapping algorithms. However, it has to be taken into account that the phase retrieval problem is not unique.

From the phase maps wavefront errors of higher order like tilt and lateral beam displacement can be computed in a similar way as outlined for the OTF based one step algorithm discussed below. However, in this study's emphasis was put on finding an algorithm, which is more suitable for a realtime implementation in a control loop than the Gerchberg-Saxton algorithm.

Optimization-based Phase Diversity Algorithm

The phase diversity algorithm is outlined briefly in section 4.4.4. For the present implementation a model based approach is used, where the complete Fresnel diffraction based optical transfer functions from the aperture to the focal plane and in parallel to the diversity plane have been implemented. Inputs of the model are the known distance between the focal and diversity plane and the estimated Zernike parameters. The Zernike parameters are found via a non-linear optimization procedure, where two algorithms have been implemented for comparison reasons. The first algorithm is the 'FMINCON' code provided by the Matlab optimization toolbox. The constrained algorithm has been used without analytical gradients, i.e. the gradients were computed numerically. The second algorithm is the 'global Direct' algorithm written by M. Bjorkman, Malardalen University, Sweden, which often finds a global minimum where FMINCON fails. Global search requires, however, a larger number of iterations than a

Astrium GmbH
88039 Friedrichshafen
Telephone: (07545) 800
Telefax: (07545) 84411

gradient based search. In order to limit the required computing effort, the resolutions of the FFTs have been limited to 256x256 pixels.

The success of an optimization process depends mainly on the characteristics of the error criterion. In the present case the diversity criterion given in [Paxman] has been implemented. In order to avoid singularities, the numerator of the criterion has been used without scaling by the denominator. The advantage of this criterion is that it is independent of the target structure, i.e. extended objects can be handled. In case of the DARWIN mission, the targets can be approximated by point sources so that from a system point of view there is no need for extended object tracking.

On the other hand the phase diversity criterion turned out to be not very well suited for an optimization process. The optimization was restricted for the following discussion to the four piston parameters. Inclusion of the four tilt parameters in the optimization resulted in an additional significant degradation of the optimization convergence. The maximal initial piston errors were obtained from a normal distribution scaled by maximal λ/4. The parameter constraints were set to 2λ, i.e. relatively narrow bounds have been used in order to limit the search space.

The best results achieved so far with a FMINCON search are shown in Figure 5.2-12. Typical piston errors without any noise and without any additional wavefront errors were in the range of 3 to 10nm. However, in many not to say most cases the optimization terminated in a local minimum. A typical result obtained with the more robust 'global Direct' method is shown in Figure 5.2-13. Although a fast convergence w.r.t. to the diversity error (reduction of nearly six orders of magnitude) and the intensities has been achieved, a considerable piston error remains. This gives a clear indication that even the global search method has been terminated in a local minimum. Using other distances between focal and diversity plane form λ/2 to f/20 did not improve the situation appreciably.

The poor convergence properties are likely caused by the implemented diversity error metric. In consequence the approach is ruled out for a fringe tracker working under realtime conditions. Whether the basic hardware setup of the diversity approach can be utilized for other fringe tracker algorithms remains to be investigated.

Astrium GmbH
88039 Friedrichshafen
Telephone: (07545) 800
Telefax: (07545) 84411

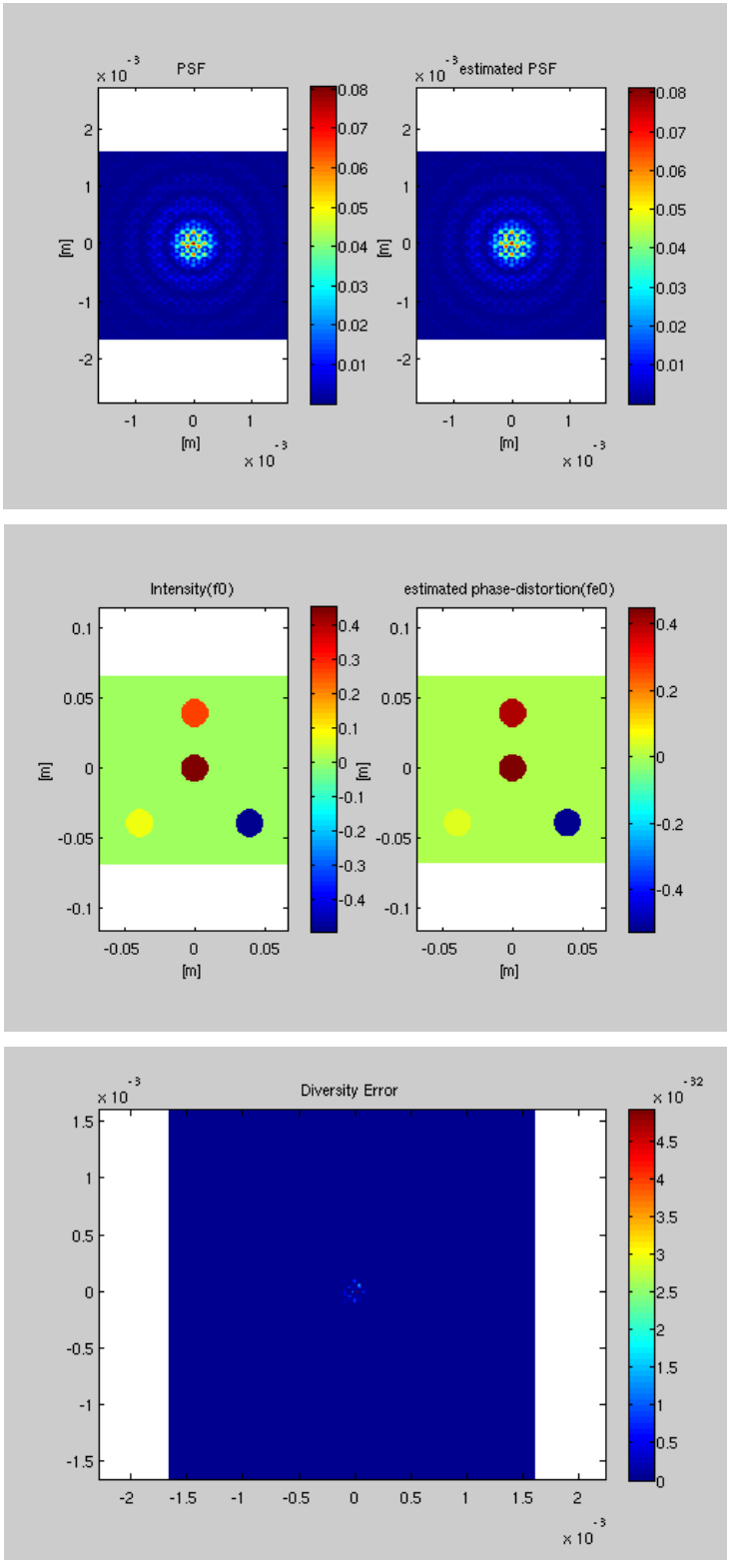

Figure 5.2-12 Best phase optimization results achieved for phase diversity (intensities, above, piston phases [~5-10nm], middle, and unscaled diversity error)

Astrium GmbH
88039 Friedrichshafen
Telephone: (07545) 800
Telefax: (07545) 84411

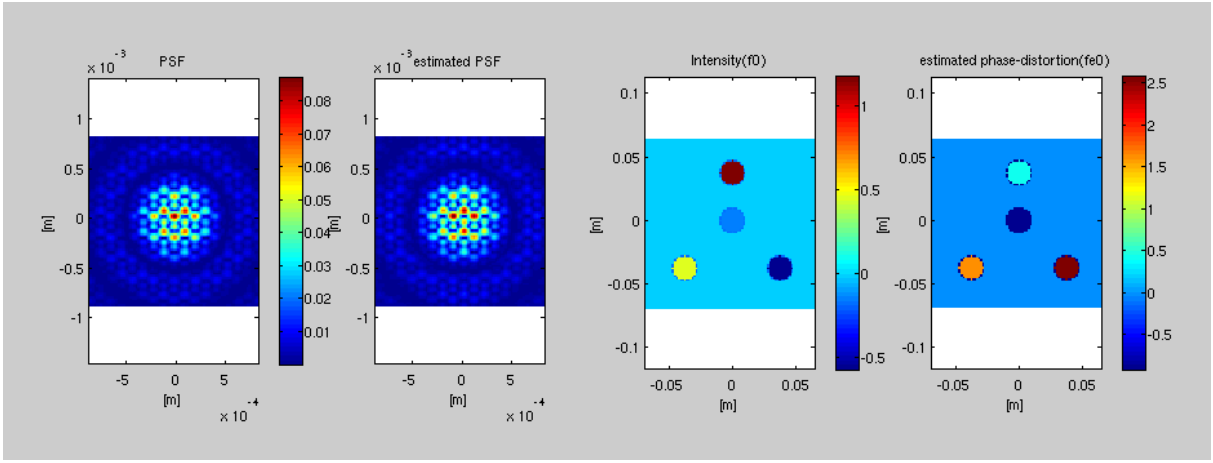

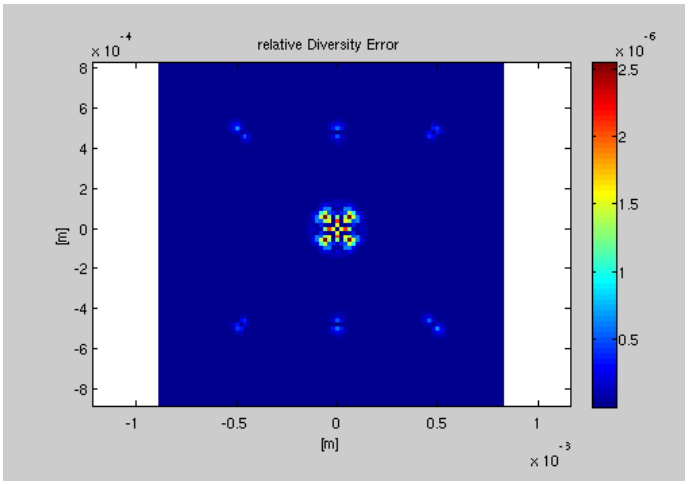

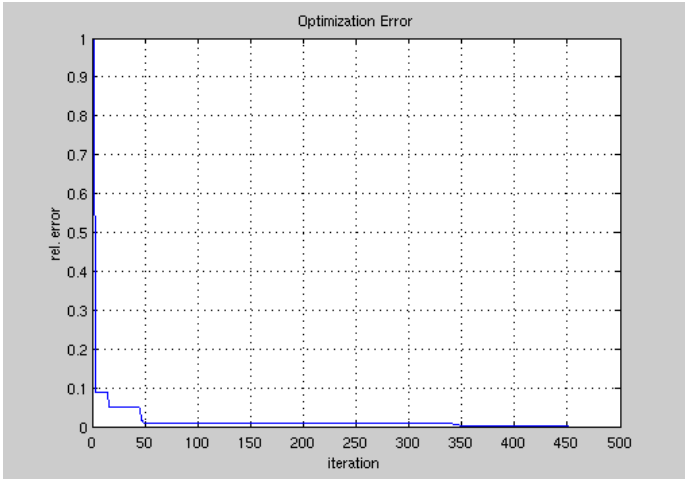

Figure 5.2-13 Local minimum with very low intensity errors but large piston errors (above left, intensities, right piston phases, middle, scaled diversity error, and below relative optimization error vs. iteration)

Astrium GmbH
88039 Friedrichshafen
Telephone: (07545) 800
Telefax: (07545) 84411

5.2.3 OTF based one step algorithm

Algorithm implementation

From a system point of view a tracking algorithm working without any iteration is desirable. A solution is given by the 'méthode rustique' [Baron], which is based on an analysis of the optical transfer function (OTF) of the system. The original method was restricted to the computation of piston errors. The algorithm described in [Baron] was adapted to the non redundant array with 4 telescopes. The piston errors are computed directly by solving an equation set via the Matlab backslash operator (least squares solution). Since the piston errors are only determined relative to each other, i.e., except a constant factor, a fourth equation has been implemented ensuring that the mean of all pistons vanishes.

Since the achieved results with this procedure were encouraging, the method has been extended within the course of this study to *tilt errors* following the same principles as for the piston errors. The major steps of the procedure are shown in the following figures.

The piston and tilt estimates are computed from the OTF-phase, which is rather noisy due to numerically caused phase wrapping effects. The information has to be obtained from the phase-map via masking functions. The centers of the masks are in the current implementation assumed to be known. They can, however, be estimated from the OTF-intensity via centroiding algorithms. Typical accurarcies of state of the art centroiding algorithms are better than 1/50 pixel for higher photon rates and may degrade to below on 1/10 pixel for low signal to noise ratios. For the application at hand accuracies of 1/10 pixel should be sufficient for phase-masking. The phase-map after masking is shown in Figure 5.2-14.

The piston and two tilt parameters are obtained on half of the phase map (the other half is redundant) via a regression for each individual mask. These values are used as inputs for two sets of equations describing the correlation between aperture windows and the related OTF-peaks w.r.t. piston and tilt wavefront errors. In absence of noise and other wavefront errors a very high accuracy can be achieved with this approach. Typical relative errors between simulated and estimated values are for both piston and tilt disturbances below 10^{-7}. However, these values degrade significantly, if phase wrapping with in each masked window arises in case of larger wavefront distortions. A typical plot with phase wrapping is shown in Figure 5.2-17. These errors can be removed, but the development of suitable procedure is not straightforward and was left to future optimization of the fringe tracker.

Astrium GmbH
88039 Friedrichshafen
Telephone: (07545) 800
Telefax: (07545) 84411

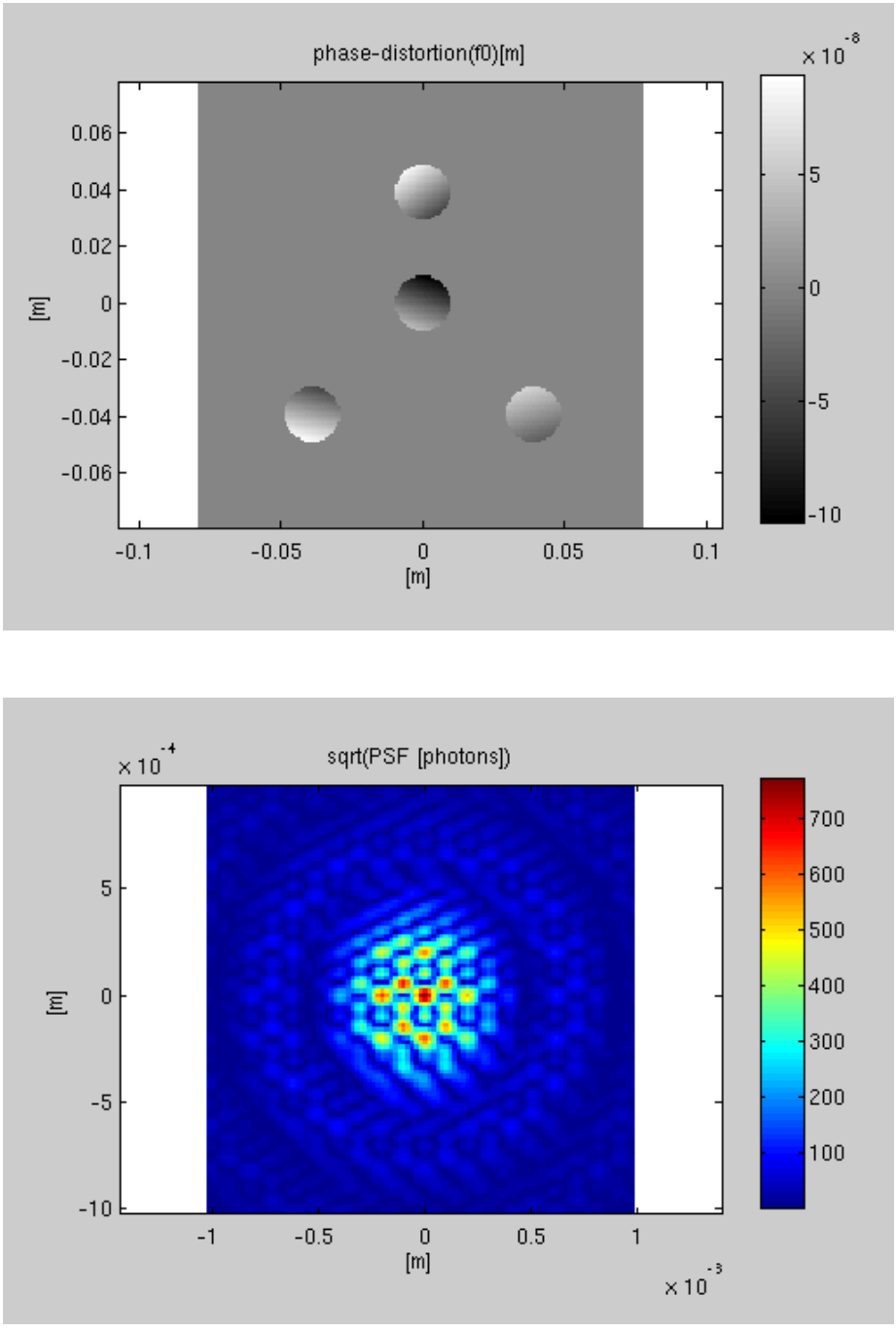

Figure 5.2-14 Simulated disturbance (random piston (λ/10) and tilt (λ/20))

Astrium GmbH
88039 Friedrichshafen
Telephone: (07545) 800
Telefax: (07545) 84411

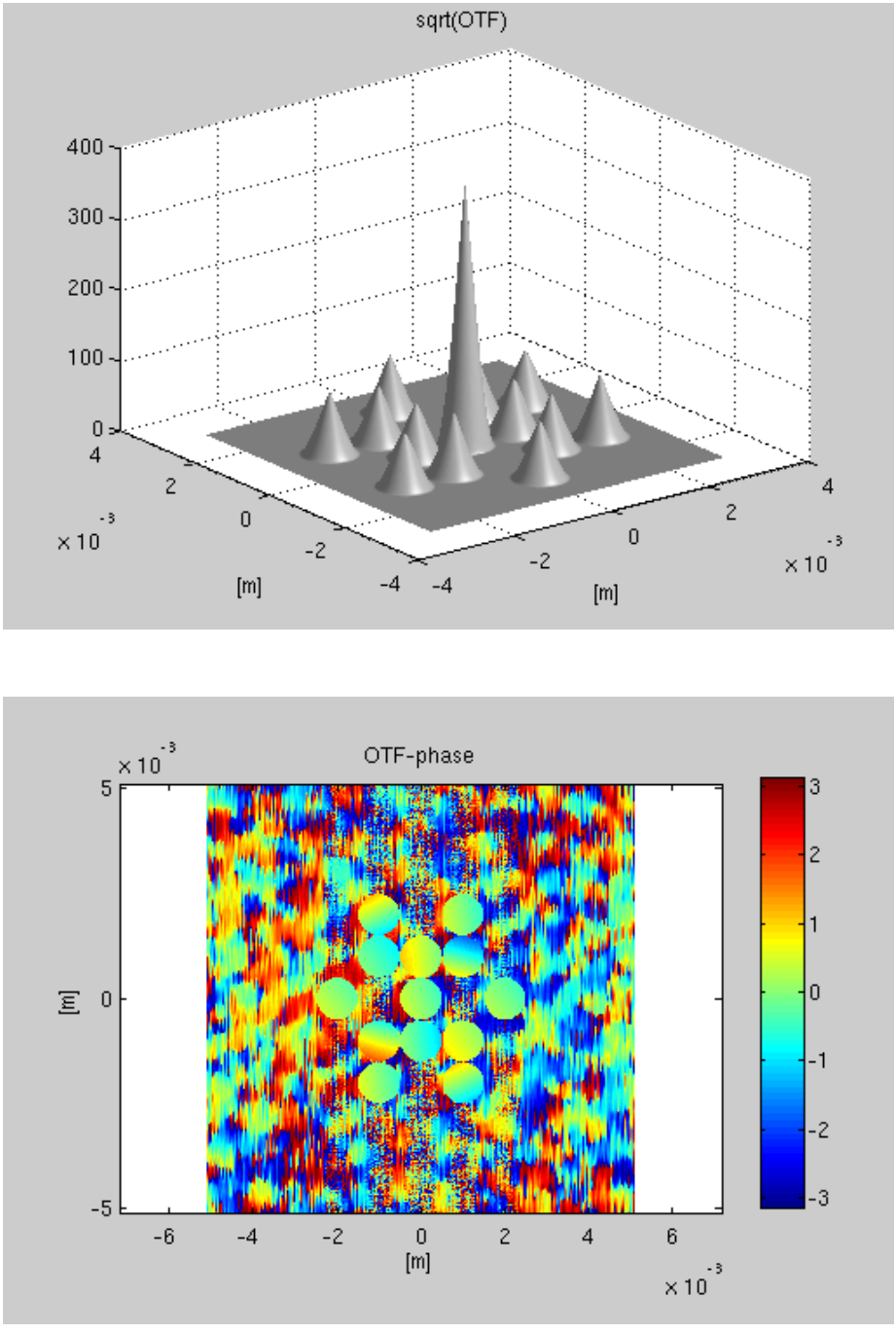

Figure 5.2-15 Computed OTF intensity (above) and OTF-phase map (monochromatic imaging).

Astrium GmbH
88039 Friedrichshafen
Telephone: (07545) 800
Telefax: (07545) 84411

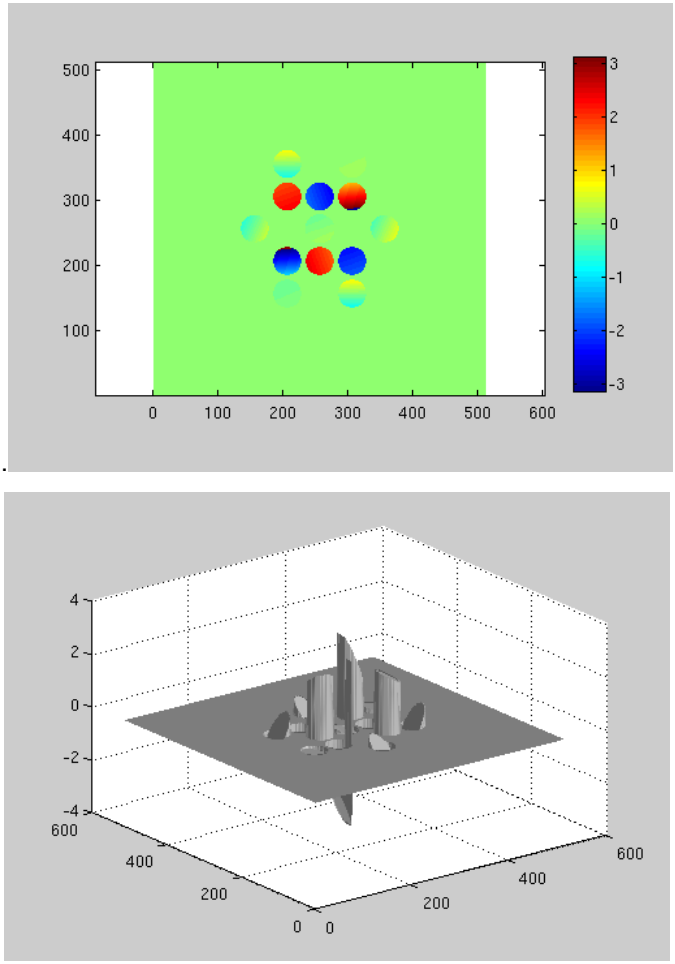

Figure 5.2-16 Masked OTF-phases (below: 3D plot of the 2D map shown above)

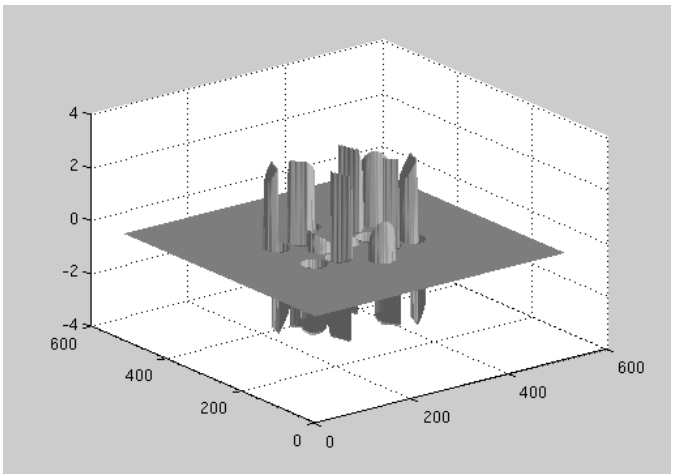

Figure 5.2-17 Phase map degraded by phase wrapping

Astrium GmbH
88039 Friedrichshafen
Telephone: (07545) 800
Telefax: (07545) 84411

Polychromatic Imaging

The images above have been computed for a mean wavelength of 660 nm. In order to evaluate the impact of a polychromatic image on the accuracy, the mean and standard deviation of the measurement errors are computed for a mv=5.6 star including photon noise. Twenty Monte-Carlo runs have been performed. The results are given in the table below.

	Piston error [nm]	**Tilt error [nm]**
monochromatic	Mean: 0.016, std.: 0.4	Mean: 0.02, std.:0.13
polychromatic	Mean: 0.011, std.: 0.38	Mean: 0.04, std.: 0.14

Table 5.2-2 Comparison of monochromatic and polychromatic repeatability without wavefront errors

The results are comparable for both runs. The fact that the piston errors are smaller in the polychromatic case than in the monochromatic one may be caused by the limited number of Monte-Carlo runs. However, other runs have shown the same tendency.

Repeatability

The repeatability of the algorithm has been computed for the nominal case without wavefront errors. Only photon noise has been taken into account. A typical plot for the piston errors is shown in Figure 5.2-18.

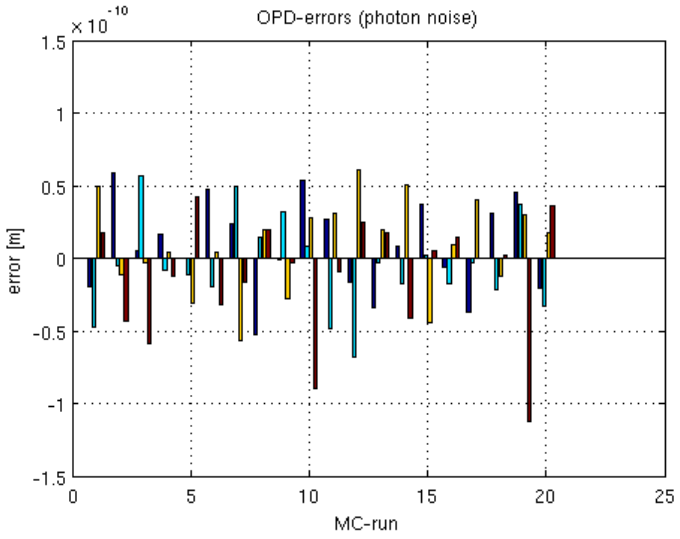

Figure 5.2-18 Monte-Carlo run for piston errors (mv=5.6 star, nominal case)

Astrium GmbH
88039 Friedrichshafen
Telephone: (07545) 800
Telefax: (07545) 84411

The results for some investigated magnitudes are listed in the table below for a polychromatic simulation, where mean values and the standard deviations are given.

Magnitude	Piston error [nm]	Tilt error [nm]
Mv= 5.6	Mean: <0.01, std.: 0.04	Mean: 0.04, std.:0.14
Mv= 9	Mean: 0.01, std.: 0.26	Mean: 0.2, std.: 0.6
Mv=12	Mean: 0.35, std.: 0.57	Mean: 0.8, std.; 2.1

Table 5.2-3 Repeatability for the nominal case

OPD linearity

As already outlined above, the piston and tilt measurement accuracy is limited by phase wrapping effects. The simulation results for a piston scan for mv=9 and mv=12 stars is shown in Figure 5.2-19 and Figure 5.2-20, where photon noise has been taken into account. In order to limit the required computing time, the curves have been calculated for the mean wavelength.

In case of the fainter star phase wrapping occurs more often than for the brighter star. The wrapping effect is much more dominant for larger tilt errors as shown in Figure 5.2-21 for a mv=12 star. The convergence range is here in the range of ~λ/10. As discussed above, unwrapping algorithms may enhance the situation.

Crosstalk of aberrations on the piston and tilt accuracy

The impact of other Zernike wavefront errors on piston and tilt errors has been investigated without photon noise. An RMS wavefront error of λ/20 has been applied to each aperture window according to a weighting vector given by [1 -1 -1 1]. The results for the maximum errors are summarized for a polychromatic simulation in the table below.

Zernike polynomial	Max. piston error [nm]	Max. x,y-tilt errors [nm]
Tilt (Z2)	0.01	-
Defocus (Z4)	14	0.9 / 0.5
Astigmatism (Z5)	0.06	0.07 / 0.14
Coma (Z8)	0.11	0.78 / 38.3
Trifoil (Z9)	0.04	0.16 / 0.84
Sperical Ab. (Z12)	5.4	0.35 / 0.21

Table 5.2-4 Impact of wavefront errors on piston and tilt accuracy

Astrium GmbH
88039 Friedrichshafen
Telephone: (07545) 800
Telefax: (07545) 84411

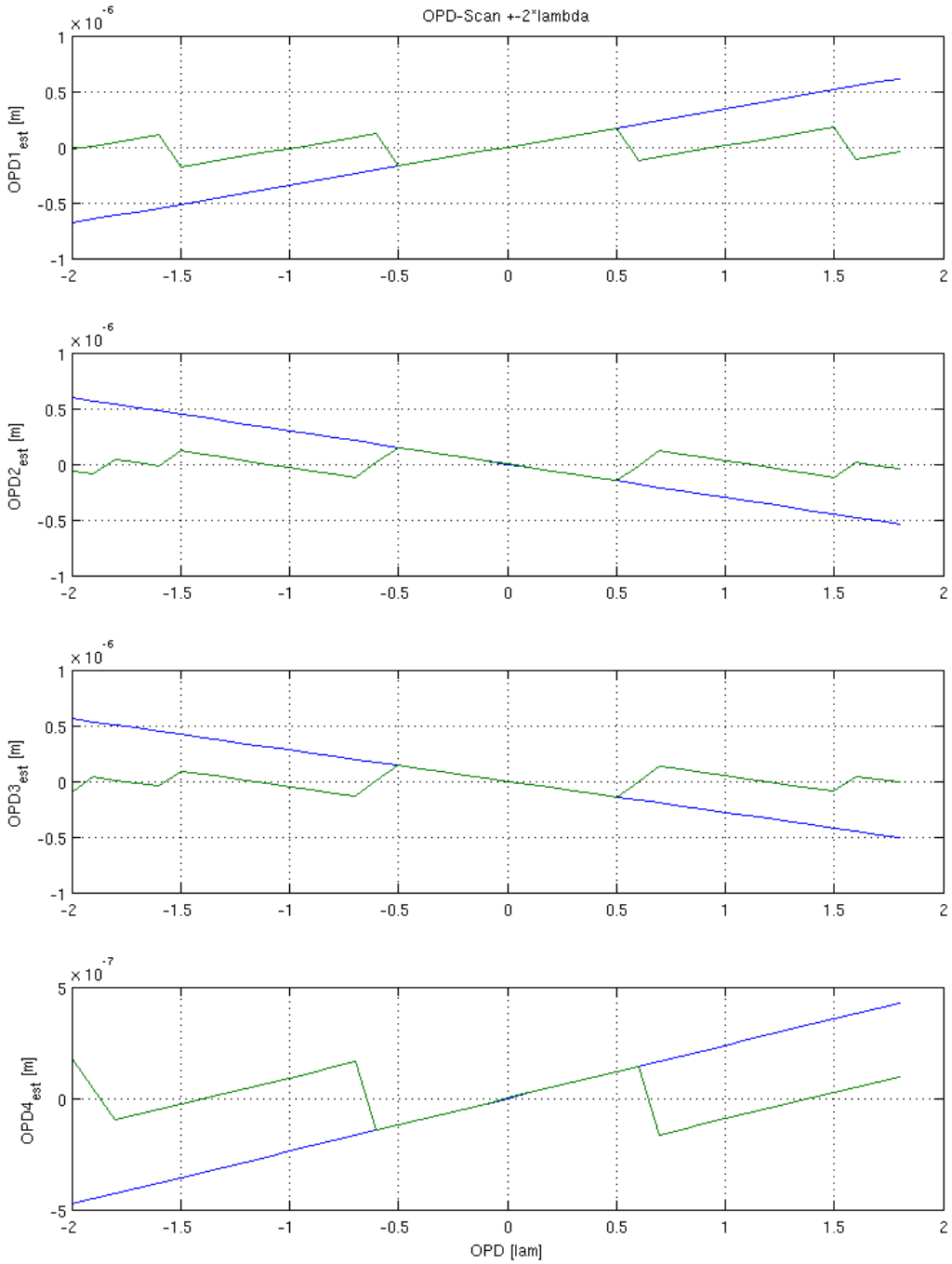

Figure 5.2-19 OPD scan for a mv=9 star

Astrium GmbH
88039 Friedrichshafen
Telephone: (07545) 800
Telefax: (07545) 84411

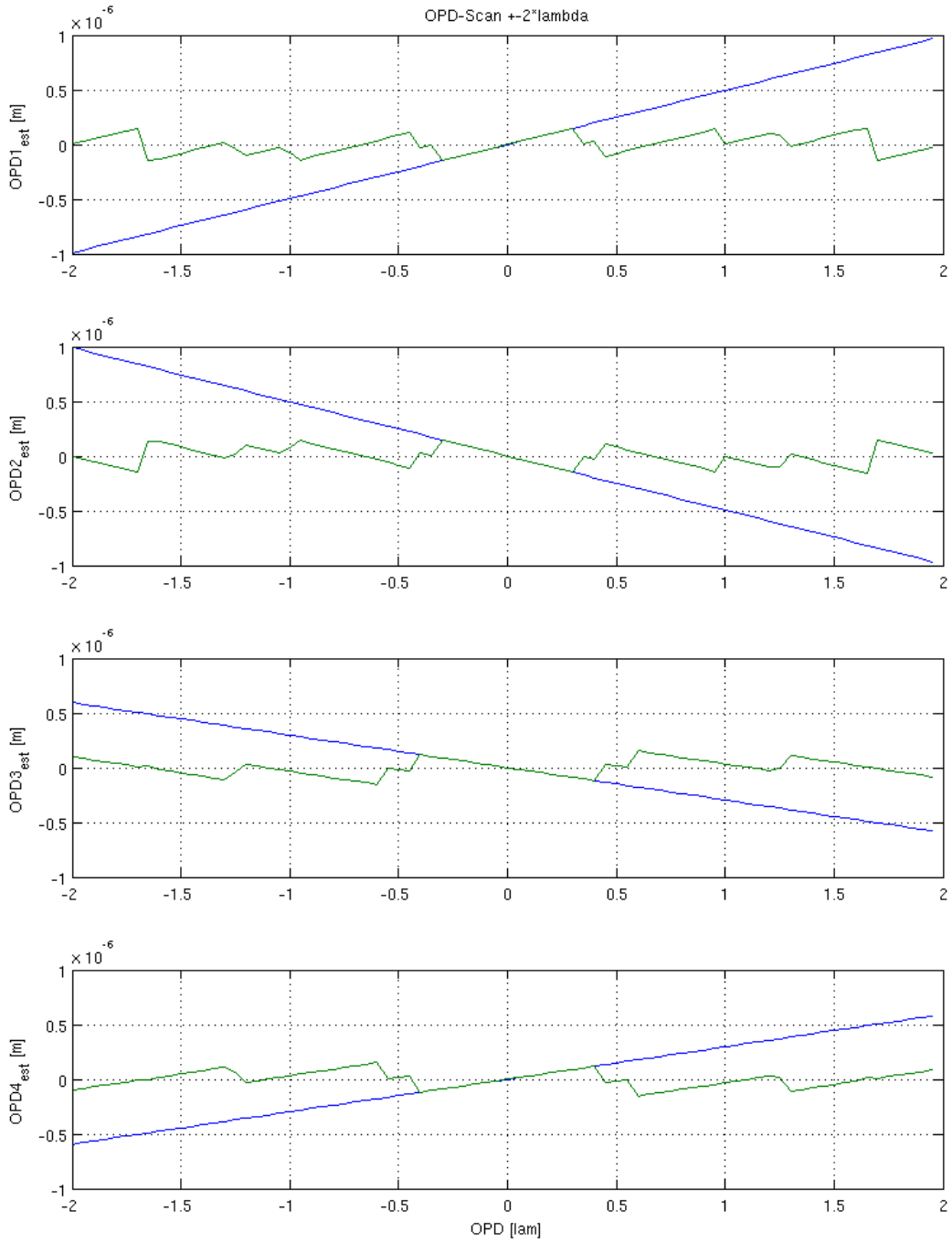

Figure 5.2-20 OPD scan for a mv=12 star

Astrium GmbH
88039 Friedrichshafen
Telephone: (07545) 800
Telefax: (07545) 84411

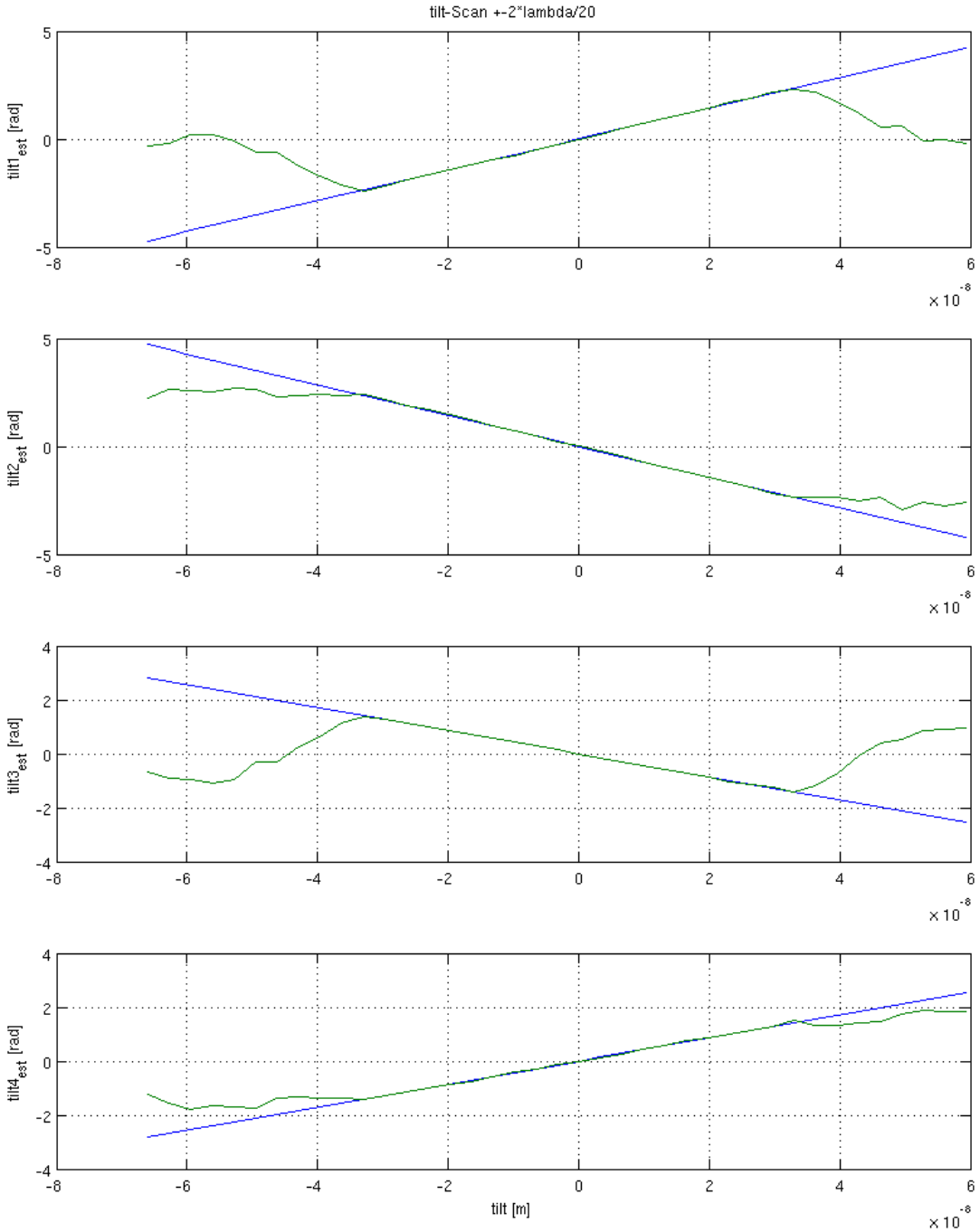

Figure 5.2-21 Tilt wavefront distortion scan

Astrium GmbH
88039 Friedrichshafen
Telephone: (07545) 800
Telefax: (07545) 84411

Due to the non-orthogonal Zernike definitions used here, defocus and sperical aberration contribute to the piston errors. Coma increases as expected the tilt error in the related axis.

Impact of lateral beam displacement on the accuracy

As discussed already above the calculation of the piston and tilt errors requires a relatively coarse alignment of the masking windows in the OTF-phase map. In the present simulation these positions are assumed to be known. The mask positions can be calculated from the OTF. Assuming an accuracy of ~1/10 of a pixel for the calculation of the OPD peaks, the related accuracy for the lateral displacements of the aperture windows would be in the range of ~40µm for 10mm beam diameter. The value is below the specifications and provides some margins for OTF degradations caused by other aberrations. This assessment has to be verified by a detailed simulation of the centroiding algorithm and the related estimation procedure for the displacements.

Iterative performance improvement

The algorithm provides the estimates without any iteration within one step. In the present implementation only standard regressions (least squares) techniques are used for the calculation of the piston and tilt estimates. Using a more refined statistical error correction mechanism may improve the results further.

The fringe tracker is operated in an iterative closed control loop, which minimizes at least the OPD and tilt errors. Provided that the tracking capabilities of the control loop are good enough, the fringe tracker is operated in nominal conditions except for fringe acquisition phases. For the detailed analysis a dynamical simulation of the overall system including the related actuators (delay lines, tip/tilt mirrors etc.) has to be set up.

Piston and tilt accuracy degradation caused by fringe smearing

During fringe acquisition fringe smearing may arise due to residual OPD velocities, which degrade the accuracy of the fringe tracker. This effect has been investigated for a noiseless case and the results are given in the table below. In the present case linear ramps from zero to the indicated peak values have been simulated.

OPD scan velocity [µm/s]	Max. Piston error [nm]	Max. x,y-Tilt error [nm]
0.33	2.1	0.06 / 0.02
0.66	4.2	0.12 / 0.05
3.3	23.6	0.7 / 0.31
8.25	60	1.8 / 0.8

Table 5.2-5 Piston and tilt errors caused by fringe smearing

Astrium GmbH
88039 Friedrichshafen
Telephone: (07545) 800
Telefax: (07545) 84411

The values given in the table are the errors compared to the maximum piston value at the end of the ramp. Taking the mean value of the disturbance would improve the results. The piston errors indicate a moderate performance degradation, which should be removed at least under steady state conditions by the OPD control system.

5.2.4 Summary and recommendations for the phase retrieval algorithms

Three phase retrieval algorithms have been investigated,

- two iterative algorithms,
  - the Gerchberg-Saxton iteration, and
  - a more general model based approach using phase diversity techniques, and finally
- a non-iterative one-step approach based on an analysis of the OTF.

The general model-based phase diversity approach requires a parameter optimization, which needs a high number of iterations and is therefore not suitable for a realtime implementation. Furthermore, the phase-diversity criterion used has a lot of local minima, where the optimization process terminates.

Much better results have been achieved with the Gerchberg-Saxton iteration, which can be seen as a prototype algorithm for a larger class of similar phase retrieval approaches. The piston and tilt estimates are computed from the retrieved phase map in a similar way as for the OTF based approach. Convergence can not be assured with this procedure. Nevertheless, due to its simplicity the approach should be retained as fall-back solution.

From a system point of view the OTF based one step algorithm is the recommended option. The original published algorithm has been extended with a tilt error estimation. A further extension to the calculation of wavefront errors of higher order and lateral beam displacements seems to be feasible. In the current implementation the algorithm is handicapped somewhat by phase wrapping effects, which have to be removed by suitable unwrapping algorithms. In case of high signal to noise ratio very high piston estimation accuracies have been achieved. The standard deviation of the piston repeatability for mv=12 stars is in the range <0.6 nm and even in this case low.

Consequently the future work should be focussed on the OTF based fringe tracker with emphasis on the following points:

- Increasing of the robustness w.r.t. phase wrapping effects
- Extension to the estimation of lateral beam displacements
- Optimization of the algorithms w.r.t. signal to noise ratio
- Extension (if required from a system point of view) to estimation of wavefront errors of higher order
- Operation of the system in a closed control loop

Astrium GmbH
88039 Friedrichshafen
Telephone: (07545) 800
Telefax: (07545) 84411

- Further performance improvements using error metrics, which take the noise statistics into account
- Enhancement of the tracking capabilities by (nonlinear) Kalman filtering of the signals
- Detection of wrong (e.g. phase wrapped) outputs of the tracker
- Verification of the performance results with a more detailed Monte-Carlo analysis

These investigations require a flexible simulation environment representing the dynamical characteristics of the whole DARWIN constellation.

Astrium GmbH
88039 Friedrichshafen
Telephone: (07545) 800
Telefax: (07545) 84411

5.3 Dispersed fringes pupil plane fringe sensor

5.3.1 Simulation model

The simulation model used to test the dispersed fringes pupil plane fringe sensor concept has been implemented in Matlab/Simulink. The model is hierarchically structured. The top level is shown in Figure 5.3-1. The model allows to introduce OPD perturbations into the two beams of the interferometer, in particular for piston and the first eleven Zernike polynomials. The model represents the interferometer in twelve spectral sub-bands. Within each sub-band the perturbed pixel-based electric fields are calculated and then superimposed in a partially coherent quasimonochromatic way. The intensity distribution resulting from the superposition is integrated such as to yield the optical power. This is done separately for both interferometer outputs. The power signals of all sub-bands are scaled with the detector integration time (20 ms) to yield optical energies. These optical energies correspond to numbers of photons. Optionally photon noise can be added. The vector of optical energies is the input to the fringe sensor algorithm that determines an OPD estimate based on it.

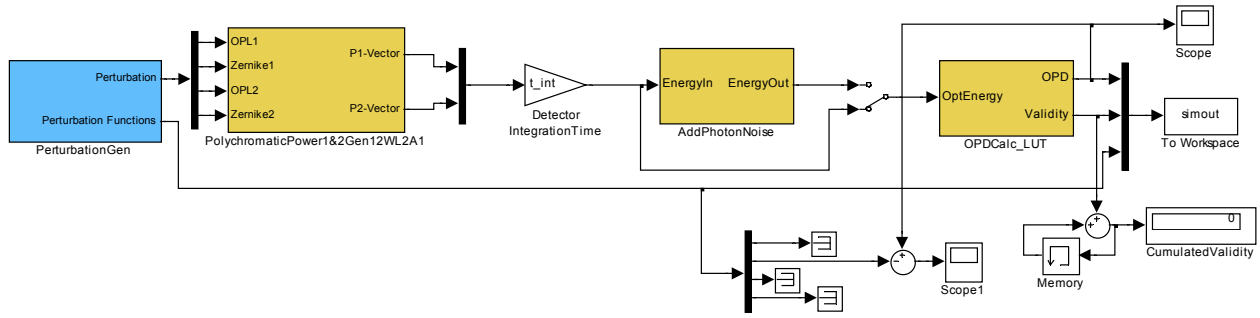

Figure 5.3-1 Toplevel Simulink model used for the test campaign. The block labelled OPTCalc_LUT contains C code in form of a Simulink S-function realising the fringe sensor algorithm. The blue submodel generates selectable deterministic and statistical beam perturbations acting on the interferometer model.

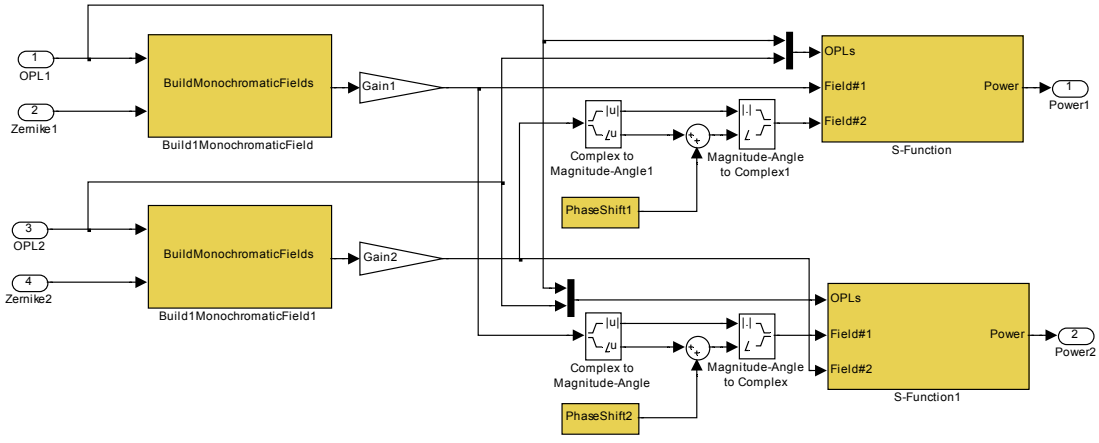

Figure 5.3-2 Electrical field generation and superposition for a single spectral sub-band.

Astrium GmbH
88039 Friedrichshafen
Telephone: (07545) 800
Telefax: (07545) 84411

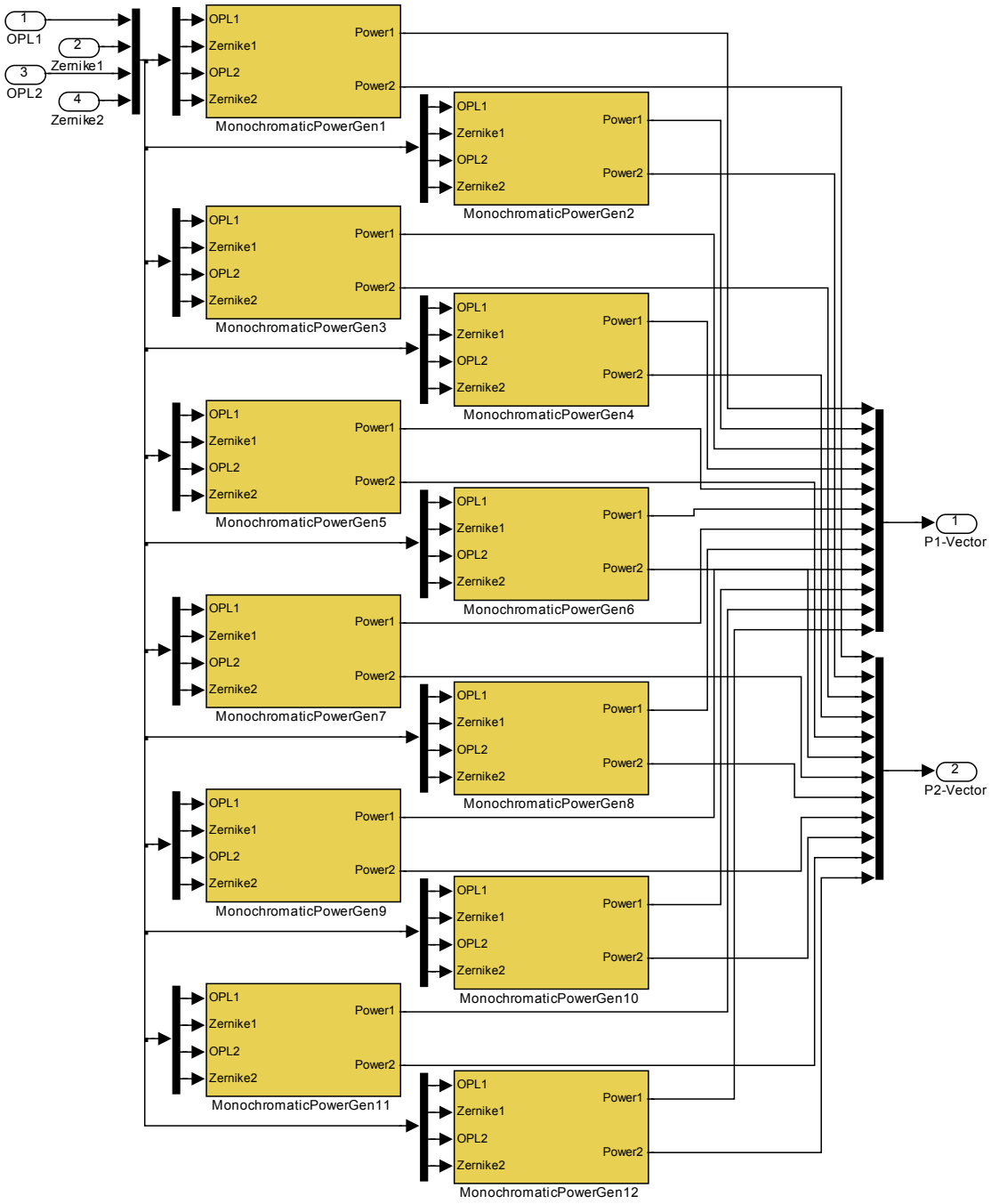

Figure 5.3-3 Interferometer model for twelve spectral sub-bands. Contents of the block labelled PolychromaticPower1&2Gen12WL2A1 in the previous figure.

Astrium GmbH
88039 Friedrichshafen
Telephone: (07545) 800
Telefax: (07545) 84411

5.3.2 Detailed fringe sensor algorithm

The fringe sensor algorithm calculates an estimate of the optical path difference (OPD) between two interferometer arms based on two sampled instantaneous complementary interferometer energy signals E1, E2 provided separately each for a set of spectral sub-bands by using a look-up table.

The fringe tracking scheme used is purely passive and doesn't require modulation of the optical path in one of the two interferometer arms. Instead, it is based on the instantaneous energy levels in the fringe patterns obtained for different sub-bands. From the instantaneous complementary energy levels E1, E2 of each sub-band a dimensionless fringe signal is derived that is normalised to the range -1 to +1.

The instantaneous normalised fringe signals of all different sub-bands used are combined to a fringe vector, the measured fringe vector. Based on a dedicated look-up table for different fringe vectors versus the corresponding OPD, an estimate of the OPD is calculated based on the measured instantaneous fringe vector using a nearest-neighbour search. For the sake of computational efficiency the nearest neighbour search is performed in two steps:

Step 1: A binary search based on the norm of the fringe vectors yields the column index i0 for the centre of the search range for Step 2. It is assumed that the norm of the fringe vectors forming part of the look-up table is contained in row 0 of this table and that this table is arranged in ascending order of this norm.

Step 2: A sequential search in the look-up table starting at the column index i0 found in Step 1 and extending over all fringe vectors, the norm of which differs by not more than specified by a parameter from the norm of the measured fringe vector. In this step the column index i within the specified

search range of the look-up table is determined for which the length of the difference between the fringe vectors is minimised. The best estimate for the OPD is extracted as last element (i.e. following the fringe vector) of column i of the look-up table. If the difference between the fringe vectors exceeds a threshold then the reconstructed OPD is flagged invalid, otherwise it is flagged valid.

It is crucial for this fringe tracking method that there exists a unique one-to-one relationship between the fringe vectors and the OPD. This constraint limits the range within which the OPD can be correctly estimated and the level of perturbations and noise that can be tolerated. On the other hand, this range can be extended however by carefully designing the set of sub-bands, e.g. by adjusting about the same coherence |ength for all of them and by using a sufficient number of spectral sub-bands spread over the fringe sensor band.

The fringe sensor algorithm requires a careful definition of the spectral sub-bands. In terms of detector pixels of the two detector arrays in Figure 4.5-1 it is necessary to decide which pixels shall be combined to represent a sub-band. We use a fringe sensor band from 600 to 1500 nm and have selected for all sub-bands the same coherence length of 12 µm. For the tests to be performed we need only the OPD range from -5 to +5 µm. The fringe signals for the 12 sub-bands within this range are depicted in Figure 5.3-4. A magnified view of the central part around zero OPD is shown in Figure 5.3-5.

Astrium GmbH
88039 Friedrichshafen
Telephone: (07545) 800
Telefax: (07545) 84411

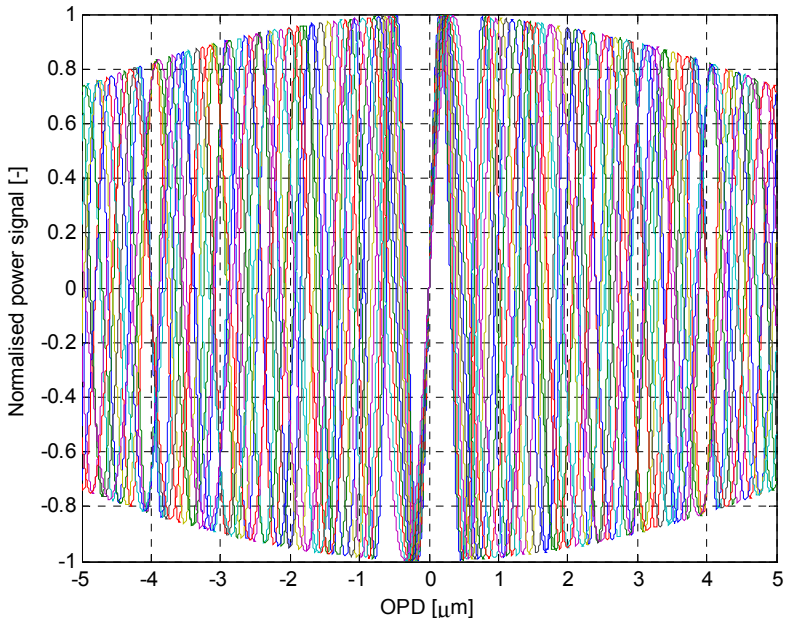

Figure 5.3-4 Normalised power signals (fringe signals) for 12 sub-bands in the range from 600 to 1500 nm with a coherence length of 12 µm each.

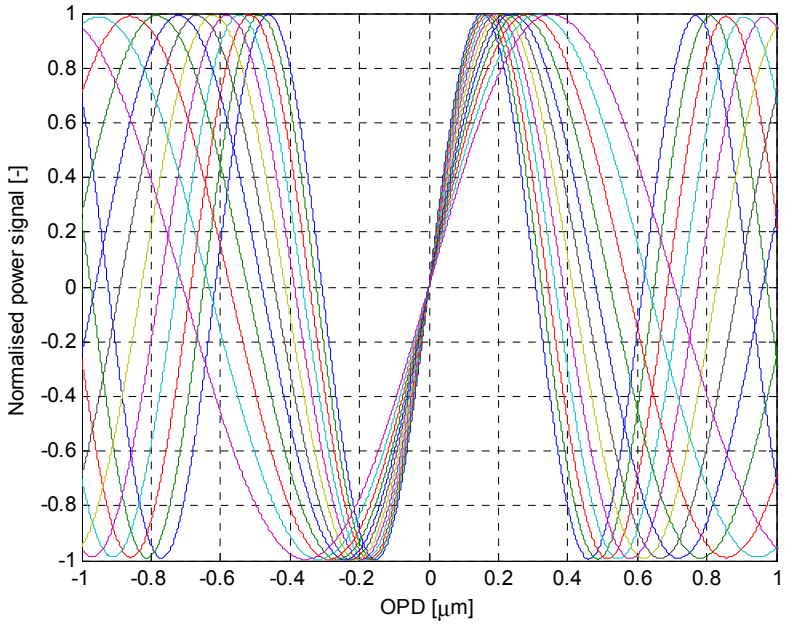

Figure 5.3-5 Magnified view of the central part of the previous figure.

The above figure shows the fringe signals close to zero OPD. We recognise that all fringe signals have a zero crossing and a steep slope for zero OPD. The steep slope is important for good OPD measurement accuracy around zero OPD. In contrast we see that in the vicinity of ±0.2 µm OPD the

Astrium GmbH
88039 Friedrichshafen
Telephone: (07545) 800
Telefax: (07545) 84411

fringe signals have vanishing slopes. We will later see that due to that the measurement accuracy will be impaired.

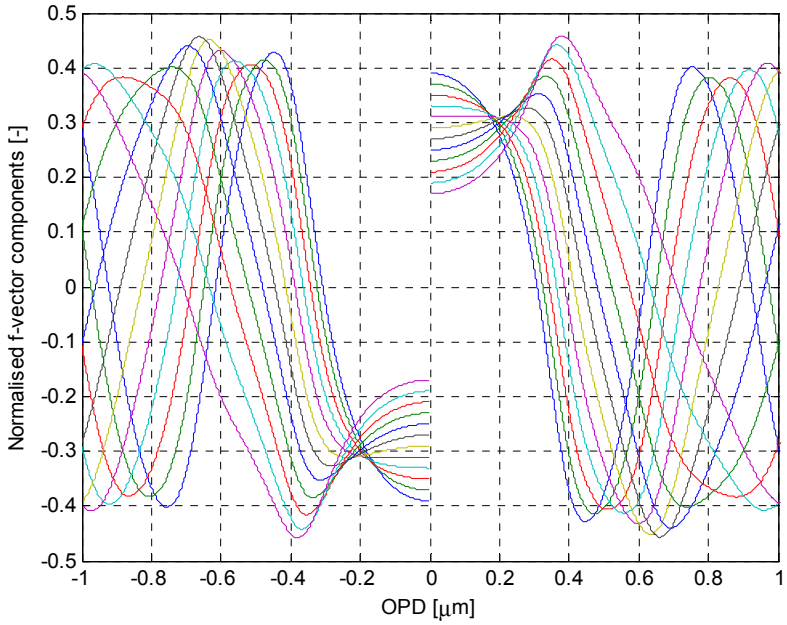

Figure 5.3-6 Normalisation of fringe vectors as unit vectors.

In Figure 5.3-6 we show an alternative way of fringe vector normalisation. Close to zero OPD the fringe signals have very small slopes and will not allow for a precise OPD reconstruction. However for OPDs above 0.3 µm the OPD reconstruction using these fringe signals is expected to be more robust. For the test campaign these alternative fringe vectors have not been used.

5.3.3 Analysis results and sensitivities

In this section we present the results of the test campaign described in section 5.1. The results obtained and described in the following paragraphs demonstrate the OPD measurement accuracy of this OPD reconstruction concept and its limitations.

A) Nominal OPD behaviour

The OPD measurement under nominal conditions, i.e. in the absence of photon noise and beam perturbations is essentially limited by the look-up table quantisation. Apart from this quantisation error the measurement is perfect. The standard deviation of the measurement error due to quantisation amounts to 0.14 nm for the selected OPD quantisation in steps of 0.5 nm. Using a finer quantisation of the look-up table would allow for a reduction of the quantisation error to even lower levels.

Astrium GmbH
88039 Friedrichshafen
Telephone: (07545) 800
Telefax: (07545) 84411

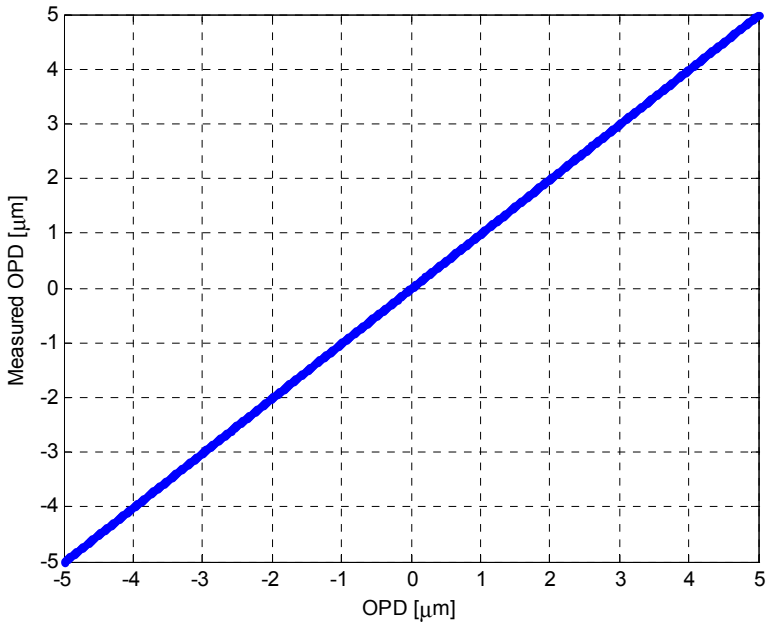

Figure 5.3-7 Measured OPD versus true OPD in the nominal case without any noise or beam perturbations.

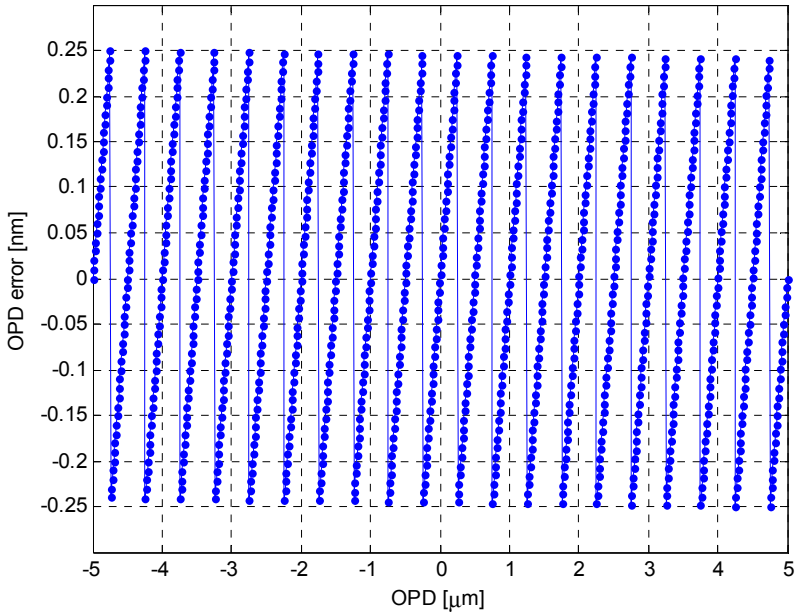

Figure 5.3-8 OPD measurement error versus true OPD in the nominal case without any noise or beam perturbations. By intentionally sampling the OPD at values different from those in the look-up table we demonstrate the effect of the OPD quantisation in the look-up table.

Astrium GmbH
88039 Friedrichshafen
Telephone: (07545) 800
Telefax: (07545) 84411

B) OPD repeatability in the presence of photon noise

The results obtained for the cases specified in 5.1 are summarised in the following table. We consider four types of target stars with different brightness ranging between third and twelfth magnitude. The OPD repeatability is analysed for two different values of OPD: for zero OPD and for an OPD of 165 nm. The value of 165 nm corresponds to $\lambda_c/4$ of the central wavelength λ_c = 660 nm in the foreseen fringe sensor band ranging from 620 to 700 nm (see section 5.1). Since we use for the fringe sensor with dispersed fringes and pupil plane beam combination a significantly wider fringe sensor band ranging from 600 to 1500 nm in order to collect more photons and since we divide this band into twelve sub-bands, the analysis of the OPD repeatability at precisely 165 nm is to some extent arbitrary.

	OPD measurement error (OPD = 0)		**OPD measurement error (OPD = 165 nm)**	
	Mean value [nm]	**Standard deviation [nm]**	**Mean value [nm]**	**Standard deviation [nm]**
m_v = 3.32	0.001	0.14	0.015	0.14
m_v = 5.65	-0.001	0.14	0	0.15
m_v = 9.0	-0.003	0.16	-0.01	0.17
m_v = 12.0	-0.003	0.33	0.008	0.41

Table 5-6 OPD measurement error due to photon noise for different target stars

We recognise from Table 5-6 that for the brightest two star types (mv = 3.32 and mv = 5.65) the resulting standard deviations of the measurement error are essentially determined by the quantisation of the OPD in the look-up table (0.5 nm) leading to a standard deviation of 0.14 nm. Only for the fainter star types (mv = 9.0 and mv = 12.0) an influence of the photon noise becomes relevant. Typical results obtained are shown in the following three figures for the faintest star with mv = 12.0 at an OPD of 165 nm.

Astrium GmbH
88039 Friedrichshafen
Telephone: (07545) 800
Telefax: (07545) 84411

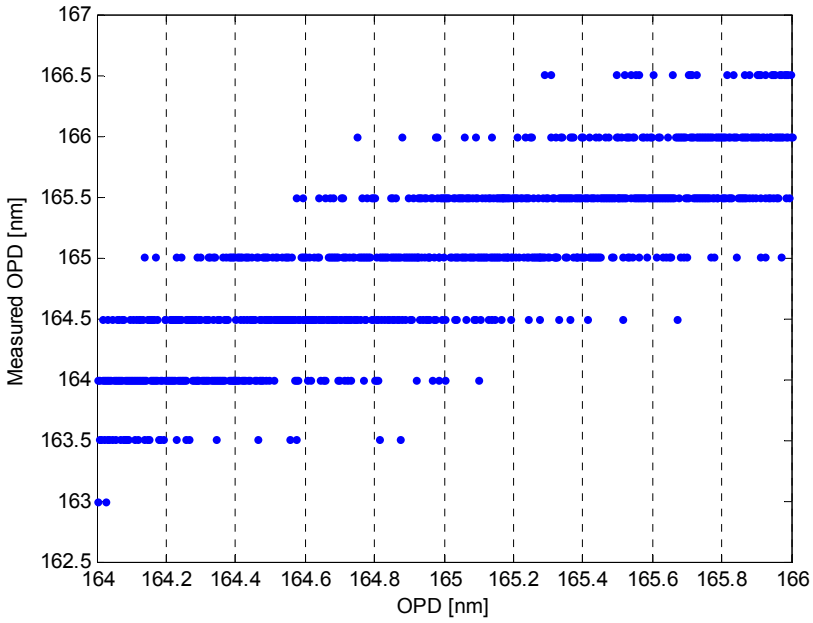

Figure 5.3-9 Measured OPD versus true OPD for m_v = 12.0 and average OPD = 165 nm. The influence of the quantisation of the look-up table is clearly visible.

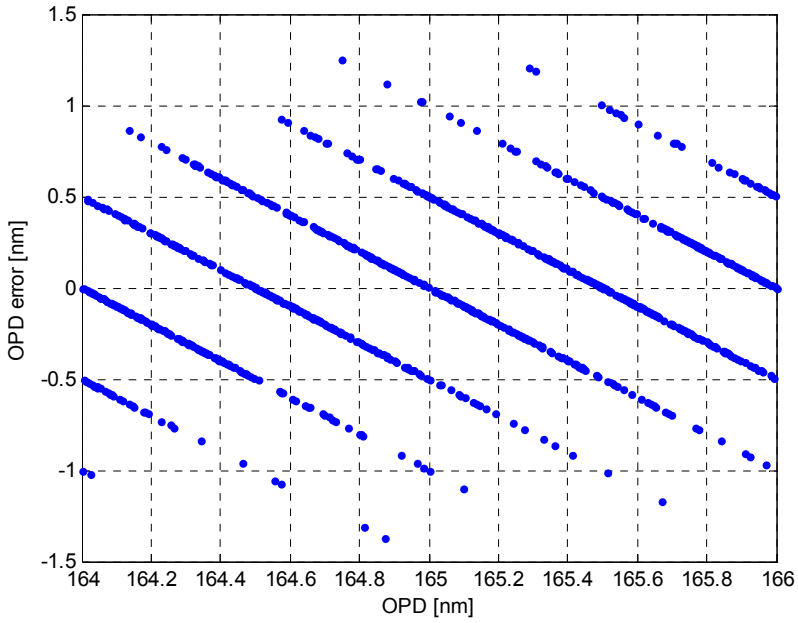

Figure 5.3-10 OPD error versus true OPD for m_v = 12.0 and average OPD = 165 nm. The influence of the quantisation of the look-up table is clearly visible.

Astrium GmbH
88039 Friedrichshafen
Telephone: (07545) 800
Telefax: (07545) 84411

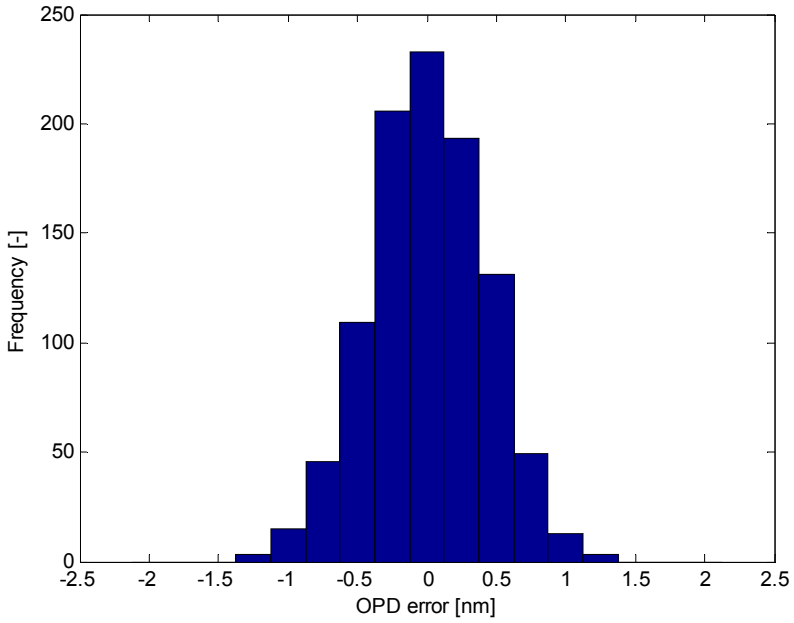

Figure 5.3-11 Histogram of the OPD error for m_v = 12.0 and average OPD = 165 nm.

C) Sensitivity against lateral beam shift

Lateral beam shift leads to imperfect overlap of the two beams. Only in the overlap area the intensity is modulated and fringes appear. In the crescent-shaped areas that are only illuminated by a single beam there is no modulation. This effect is clearly visible in the following figure.

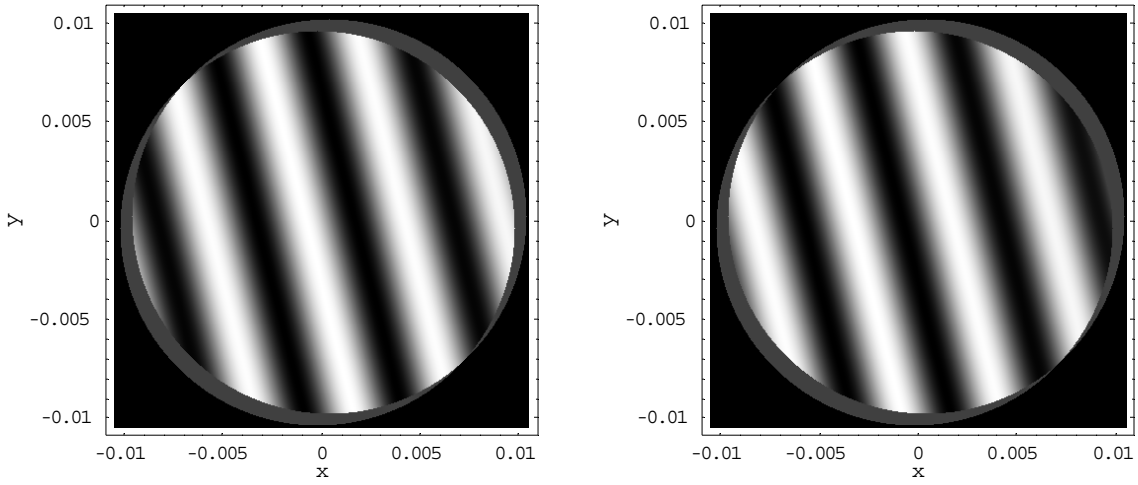

Figure 5.3-12 Pupil plane fringe patterns in the presence of lateral beam shift and beam tilt. The narrow crescent-shaped areas of no overlap are grey. The two plots show the constructive and the destructive interferometer outputs with a π phaseshift in between. Such patterns can be observed at the left and right exit of the beam combiner in Figure 4.5-1.

Astrium GmbH
88039 Friedrichshafen
Telephone: (07545) 800
Telefax: (07545) 84411

When integrating over the pupil plane the resulting power signals are reduced in fringe contrast due to imperfect overlap. For a total lateral beam offset of 0.6* √2 = 0.85 mm this leads to a not insignificant reduction in the normalised power signals of about 11 percent.

The influence of a lateral beam shift of 0.6 mm on the OPD measurement error is demonstrated in the following figures. The beam shift leads to a marked measurement error. Around +200 nm and around -200 nm OPD the error peaks. This is due to the similar values and small gradients of the fringe signals for these values of OPD. For control purposes the OPD measurement is nevertheless well suited. It vanishes precisely for zero OPD and is monotonuously increasing with increasing OPD as can be seen from the ensuing figures.

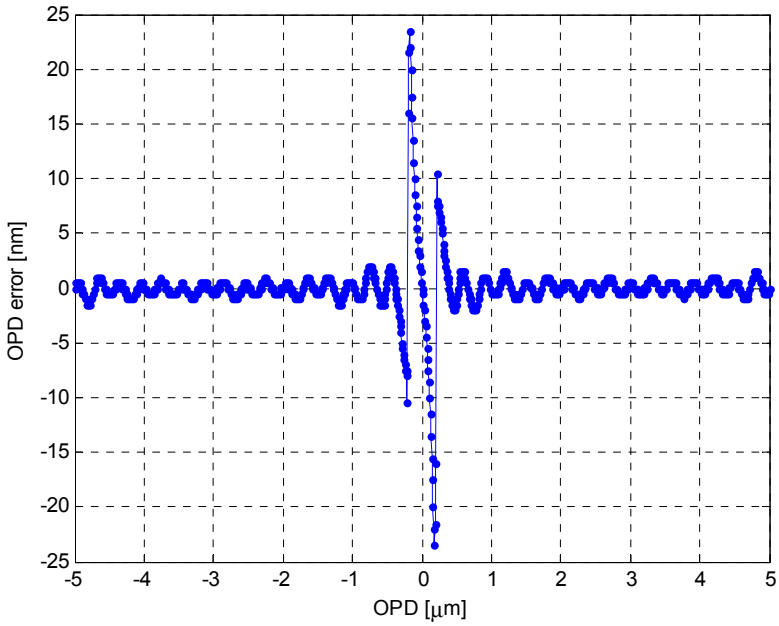

Figure 5.3-13 OPD measurement error during an OPD scan with maximum beam offset (0.6 mm)

Astrium GmbH
88039 Friedrichshafen
Telephone: (07545) 800
Telefax: (07545) 84411

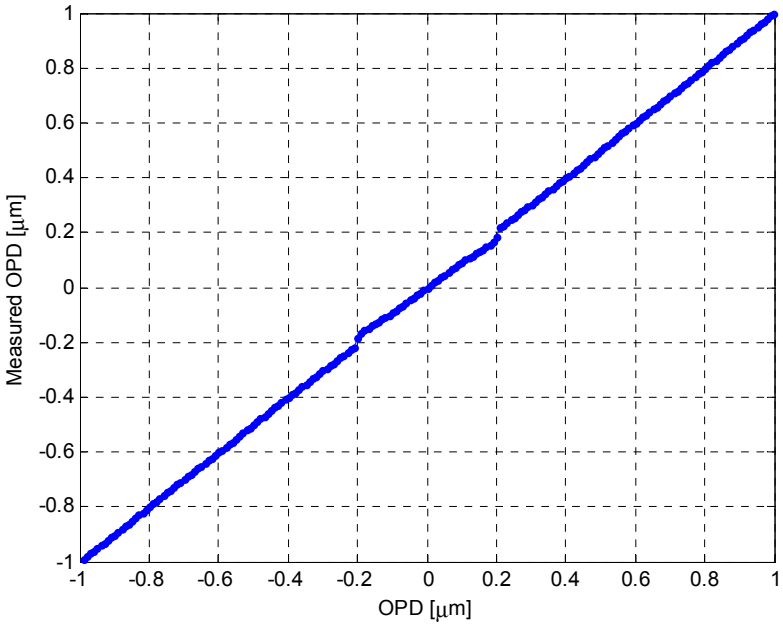

Figure 5.3-14 Measured OPD versus true OPD during an OPD scan with maximum beam offset (0.6 mm).

D) Sensitivity against beam tilt

The influence of beam tilt on OPD measurement error is shown hereafter. First of all we consider a static tilt acting on both beams (+2.8 arcsec on Beam 1, -2.8 arcsec on Beam 2) and perform an OPD scan.

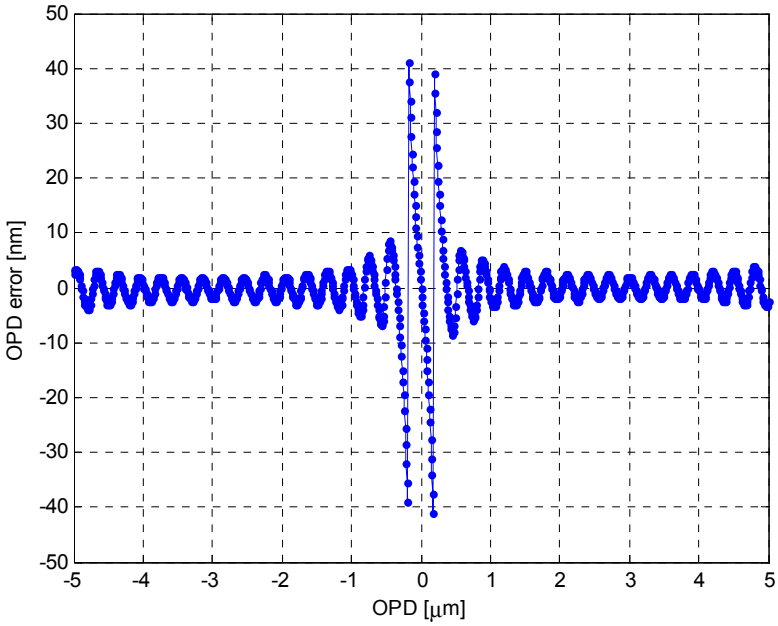

Figure 5.3-15 OPD measurement error versus true OPD in the presence of beam tilt of +2.8 arcsec on Beam 1 and of -2.8 arcsec on Beam 2.

Astrium GmbH
88039 Friedrichshafen
Telephone: (07545) 800
Telefax: (07545) 84411

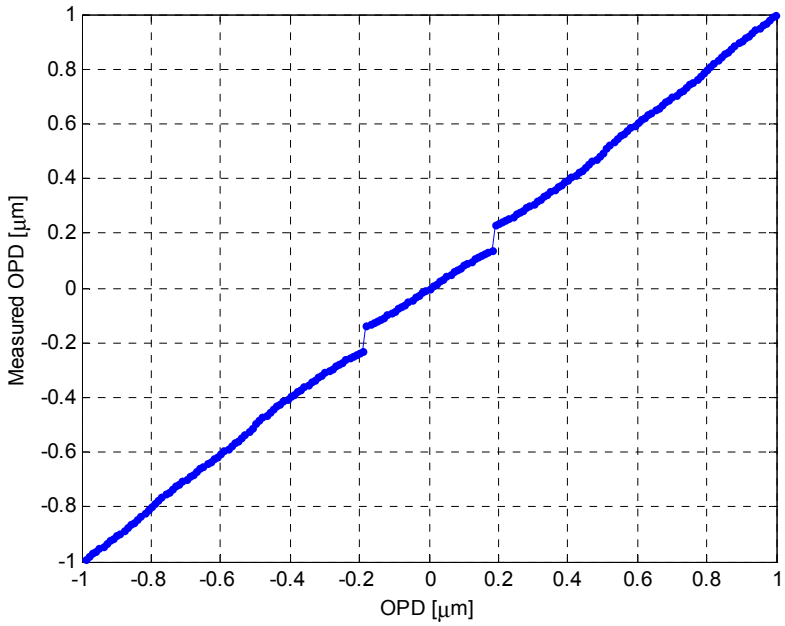

Figure 5.3-16 Measured OPD versus true OPD in the presence of beam tilt of +2.8 arcsec on Beam 1 and of -2.8 arcsec on Beam 2.

Next we double the static tilt acting on both beams (+5.6 arcsec on Beam 1, -5.6 arcsec on Beam 2) and perform an OPD scan. We recognise that for OPDs ranging from -1 to -0.5 µm and from +0.5 to +1 µm the OPD reconstruction fails now.

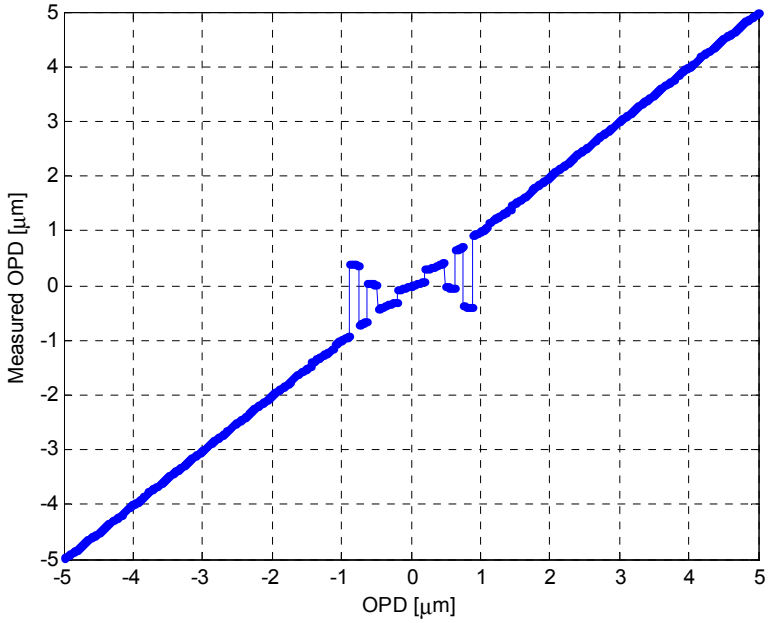

Figure 5.3-17 Measured OPD versus true OPD in the presence of beam tilt of +5.6 arcsec on Beam 1 and of -5.6 arcsec on Beam 2. The OPD reconstruction partly fails.

Astrium GmbH
88039 Friedrichshafen
Telephone: (07545) 800
Telefax: (07545) 84411

We demonstrate now the influence of random beam tilt variations on both beams with a mean value of + 1.4 arcsec for Beam 1 and of -1.4 arcsec on Beam 2. On top of these mean tilts we apply normally distributed tilts with a standard deviation of 1.4 arcsec.

We consider two cases: zero OPD and OPD = 165 nm. For both cases we use the same set of random tilts that are characterised by the histograms in Figure 5.3-18.

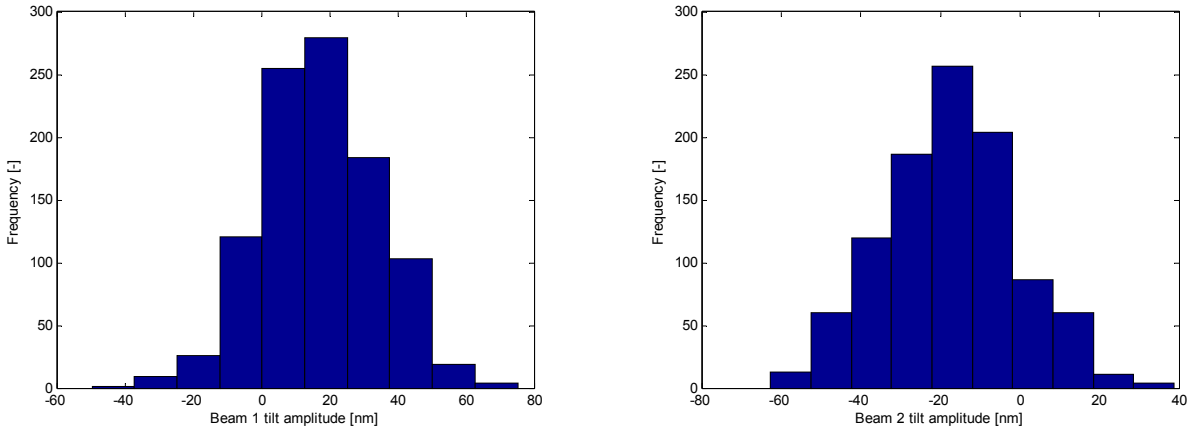

Figure 5.3-18 Random beam tilts applied to Beam 1 and Beam 2. The two histograms show the *rms* tilts in units of nanometers over the beam cross section since we use a set of Zernike polynomials normalised so as to feature a unity rms value. For a 10 mm diameter beam a beam tilt of 1.4 arcsec hence translates into an rms Zernike amplitude of 0.005*tan(1.4 arcsec)/2 = 17.0 nm.

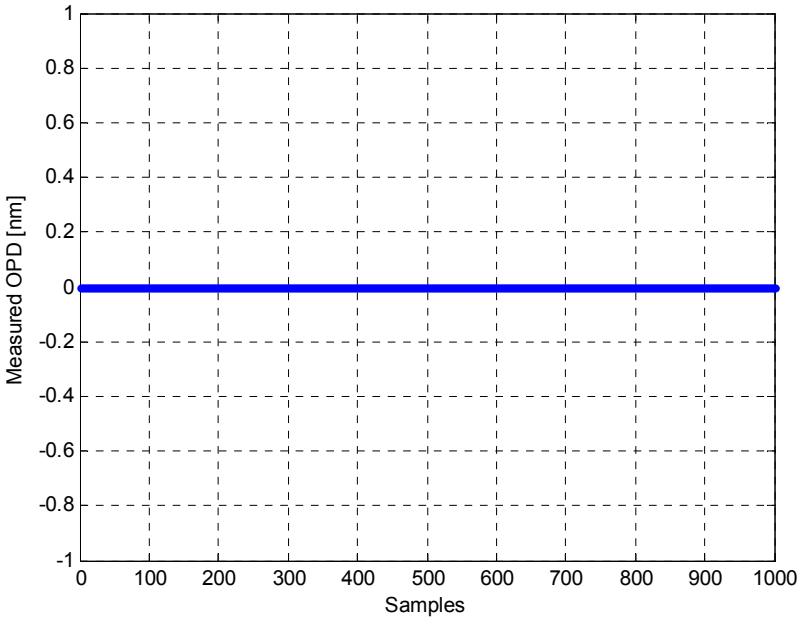

Figure 5.3-19 OPD measurement error at zero OPD for 1000 random beam tilts. The measurement error is *perfectly* zero!

Astrium GmbH
88039 Friedrichshafen
Telephone: (07545) 800
Telefax: (07545) 84411

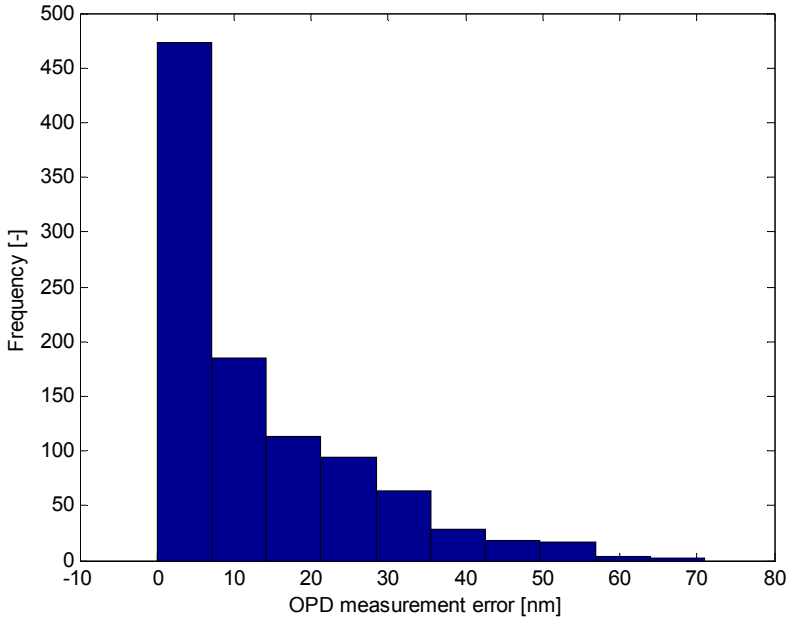

Figure 5.3-20 Histogram of the OPD measurement error (true OPD minus measured) for OPD = 165 nm in the presence of random beam tilts. The error is one-sided: the measured OPD is always smaller than the true OPD. Mean error = 12.7 nm, standard deviation = 13.3 nm.

E) Sensitivity against higher order aberrations

The sensitivity of the OPD measurement error against higher order wavefront aberrations of the two beams has been analysed separately for defocus Z4, astigmatism Z6, coma Z8, spherical aberration Z9 and trefoil Z10. In the cases analysed we have always performed an OPD scan over the full OPD range from -5 to +5 µm. On Beam 1 a Zernike RMS amplitude of +20 nm has been applied and on Beam 2 of -20 nm. The resulting measurement error and its dependency on the true OPD is visually indistinguishable. For this reason we show hereafter only the results for defocus.

As already encountered for tilt and beam shift we recognise the error peaking at +200 nm OPD and at -200 nm OPD. For zero OPD the measurement error is precisely zero.

Astrium GmbH
88039 Friedrichshafen
Telephone: (07545) 800
Telefax: (07545) 84411

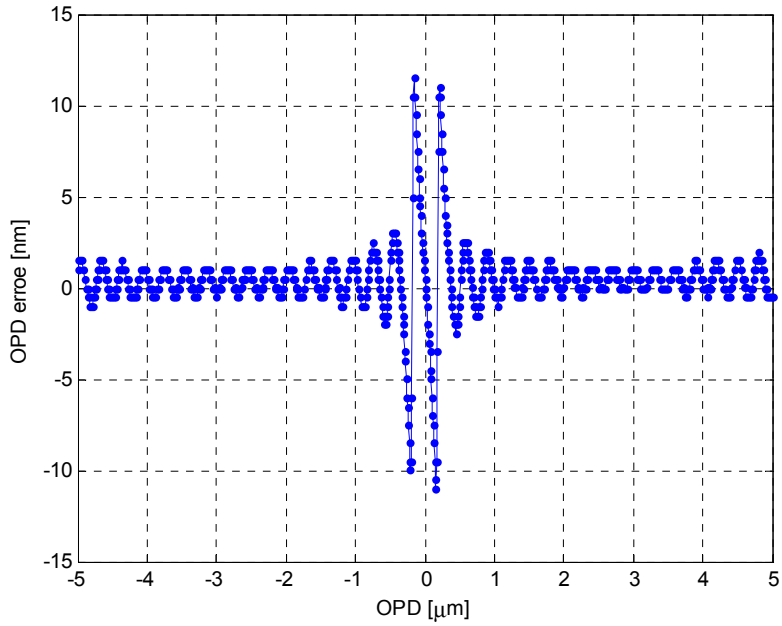

Figure 5.3-21 OPD measurement error versus true OPD in the presence of +20 nm (rms) defocus on Beam 1 and of -20 nm (rms) defocus on Beam 2.

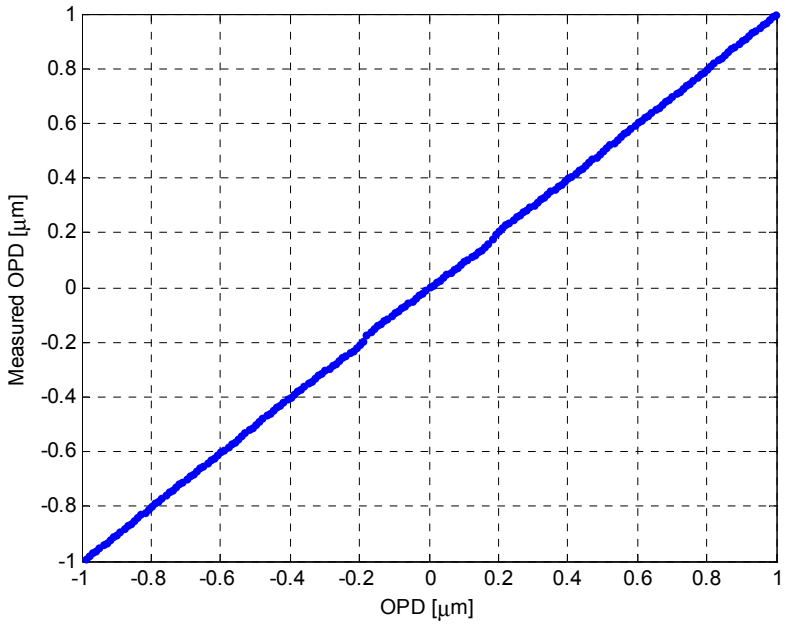

Figure 5.3-22 Measured OPD versus true OPD in the presence of +20 nm (rms) defocus on Beam 1 and of -20 nm (rms) defocus on Beam 2. Magnified view of the OPD range from -1 to +1 µm.

Astrium GmbH
88039 Friedrichshafen
Telephone: (07545) 800
Telefax: (07545) 84411

F) Sensitivity against fringe smearing

We have performed simulation runs with three different scan rates. For scan rates of 1 µm/s and of 2 µm/s the results are shown hereafter. For a scan rate of 4 µm/s the OPD reconstruction failed.

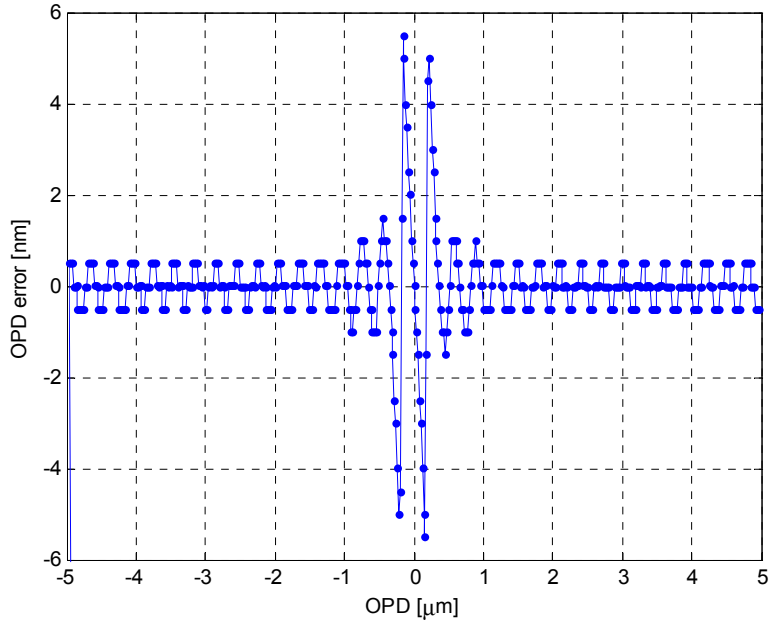

Figure 5.3-23 OPD measurement error during a scan with a scan rate of 1 µm/s.

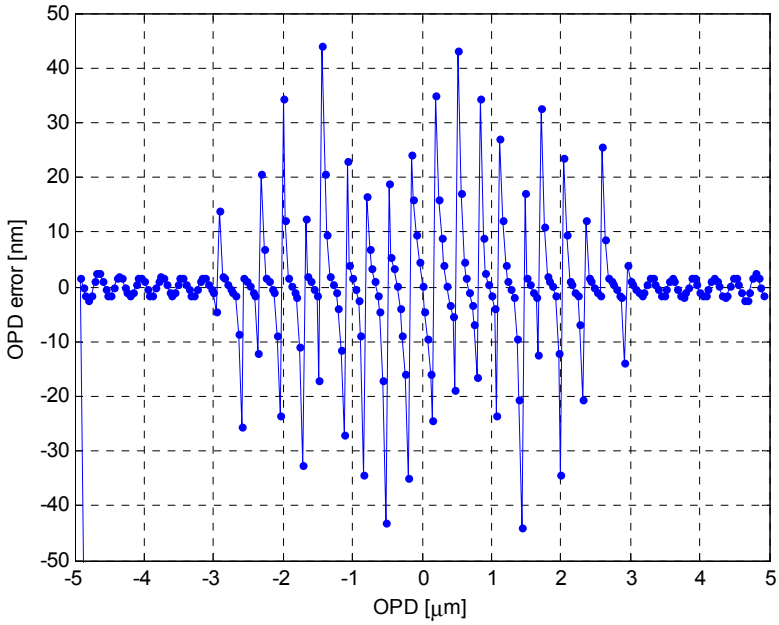

Figure 5.3-24 OPD measurement error during a scan with a scan rate of 2 µm/s.

Astrium GmbH
88039 Friedrichshafen
Telephone: (07545) 800
Telefax: (07545) 84411

G) Concluding remarks

- Robust fringe sensing method with very small measurement error at zero OPD
- Influence of photon noise is virtually negligible.
- For high beam tilts or OPD scan rates the OPD reconstruction fails
- Scan rates up to 2 µm/s are supported
- The combination of the two different fringe vector normalisation methods appears well suited to further increase the robustness of the method. An open point is the criterion to use for switching between the two methods.
- The method needs to be checked for fringe acquisition *outside* the +/-5 micron OPD range, e.g. when an OPD scan is performed and far out fringes (beyond the coherence length) are detected.
- The method needs to be extended to provide a validity flag indicating that the current OPD measurement is valid or not.
- The method is well suited for OPD ranges far greater than +/-5 µm and could also be fitted to the originally foreseen FSU band from 620 to 700 nm. In this case the coherence length and thus the OPD measurement range could be significantly increased. But the influence of photon noise will be more marked.
- For each pair of beams a separate fringe sensor is necessary. For four beams this yields six fringe sensors. Of course, these six sensors can be combined into a single unit. The OPD results of these sensors are partly redundant (four out of six) and the redundancy can be used for checking the validity of the OPD measurements.

Astrium GmbH
88039 Friedrichshafen
Telephone: (07545) 800
Telefax: (07545) 84411

6 Study Results and Future Prospects

6.1 Results

This study has analyzed the current baseline fringe sensor approach for DARWIN and one alternative. This baseline approach is based on a non-dispersed image plane beam combination which generates a complex fringe (“Interferenzstreifen”) pattern.

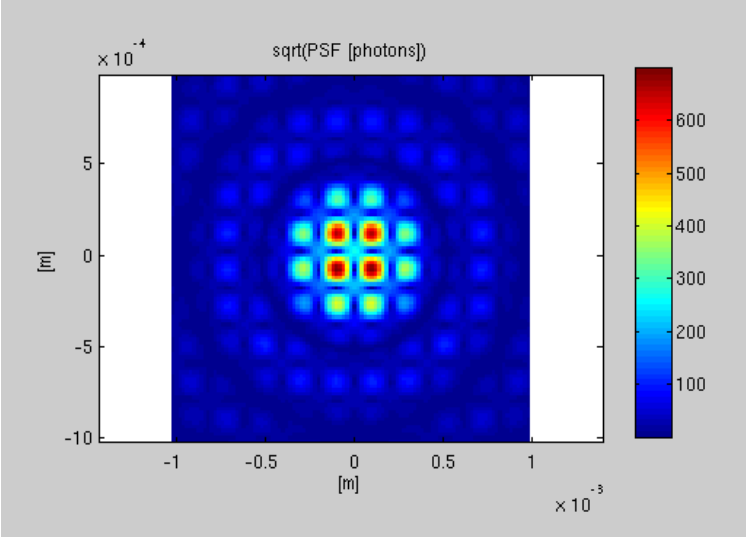

Figure 6.1-1 White light/non-dispersed fringe pattern in image plane

For this image plane approach, phase distributions of the original four beams were reconstructed by three algorithms:

- One step reconstruction based on analysis of the optical transfer function OTF, allowing for reconstruction of OPD, tip/tilt, and lateral beam displacement
- Iterative reconstruction based on phase retrieval in a single image plane, allowing for reconstruction of OPD, tip/tilt, and higher Zernikes.
- Iterative reconstruction based on phase diversity in one focussed and one intentionally defocussed image plane, allowing for reconstruction of OPD, tip/tilt, and higher Zernikes without sign ambiquitites (not further analyzed in detail due to convergence problems).

One-step reconstruction based on OTF

This approach compares the Fourier transform of the image with the autocorrelation function of a parametric model of the aperture plane wavefronts, and indentifies OPD, tip/tilt, and lateral beam displacement with sufficient accuracy and SNR. It is sensitive with respect to defocus for OPD reconstruction, and to coma for tip/tilt reconstruction. Since these higher order aberrations are expected to be static only for DARWIN, they only provide a constant bias in the fringe sensor output, which can be calibrated out on system level.

Astrium GmbH
88039 Friedrichshafen
Telephone: (07545) 800
Telefax: (07545) 84411

Though this is an extension of an existing algorithm [Baron] for solely OPD reconstruction, it is in itself a new algorithm with new functionality of tip/tilt and lateral beam displacement reconstruction. In combination with the below phase retrieval algorithms it is a very versatile and promising approach.

Phase retrieval and phase diversity with moderate computation effort

The achievable accuracy for phase retrieval and phase diversity with moderate computation effort turned out not to be compatible with the DARWIN sub-nm requirements. Nevertheless, since this algorithm requires no hardware modifications to the one-step reconstruction, it provides a very useful add-on for robust determination of higher order wave-front errors and can play an important backup role for optical FDIR (fault detection, isolation, and recovery) purposes, like quantification of optical misalignment etc.

The spectral bandwidth limitation for all these image plane non-dispersed algorithms is around 15%, which provides just significant photon-noise limited SNR to fulfil the reproducibility requirements with current understanding

Alternative approach

For comparison, a complementary approach for an alternative DARWIN fringe sensor has been studied, relying on pupil plane beam combination and spectral dispersion. The main advantage is that it allows for much higher spectral bandwidth and therefore SNR. But it only allows for OPD reconstruction, not for separate reconstruction of tip/tilt, beam displacement or higher order wavefront aberrations. It is expected that this approach has intrinsically higher sensitivity to drift of detectors and electronics than the image plane approach.

Conclusion

The principal feasibility of all the above approaches for DARWIN requirements has been demonstrated except for the current implementation of the model-based phase diversity algorithm. Nevertheless it is still substantial work to make them really robust and to optimize their performance. In subsequent phases, the tasks to be tackled further are:

- Systematic phase unwrapping for phase retrieval
- Closed loop simulations for actual acquisition of zero OPD, the nominal working point
- Monte-Carlo simulations with all perturbations simultaneously
- Error handling and validity of signal tagging

6.2 Future prospects

DARWIN fringe sensor selection and algorithm refinement

None of the studied fringe sensor designs and algorithms shows an ideal response over the full coherence length of ±4 µm, rather each one exhibits specific deviations within the coherence length which have to be taken into account specifically for closed loop simulation of DARWIN science signal acquisition.

Astrium GmbH
88039 Friedrichshafen
Telephone: (07545) 800
Telefax: (07545) 84411

Therefore a final decision/trade can only be undertaken following

- Detailed closed loop control simulations of fringe acquisition for each specific fringe sensor type
- Detailed closed loop control simulations for random peturbations in DARWIN science mode for each specific fringe sensor type
- Precise specification of DARWIN environment on system level, especially microvibrations from cryogenic coolers and micropropulsion/FEEPS
- Detailed physical modelling of critical elements like detector sensitivity, drifts, etc.

Furthermore refinement of the algorithms in terms of phase unwrapping and validity tagging is highly recommended.

We propose to continue the study in 2007 into this direction.

Phase retrieval and phase diversity applications

The algorithms developed herein are useful beyond their special applicability to DARWIN. For all critical future optical missions with an image plane sensor, they provide a robust solution for determining wavefront errors in orbit. A possible application could be LISA, the laser interferometer space antenna for gravitational waves.

A further foreseeable application is phasing of large segmented mirror telescopes, e.g., the European Extremely Large Telescope. Though there are other faster applicable techniques for phasing of dense arrays (which DARWIN is NOT), our implemented phase retrieval algorithms provide a robust complementary alternative. Another potential application might be an alternative phasing approach for the two 8.2m mirrors of LBTI (large binocular telescope interferometer) where currently the development of an interferometric science beam combiner is under work at MPIA Heidelberg and MPIfR Bonn.

We intend to contact the involved parties and to discuss possibilities of collaboration with them for possible continuation of phase diversity activities into these directions, too.

Astrium GmbH
88039 Friedrichshafen
Telephone: (07545) 800
Telefax: (07545) 84411